Control Design for Long Endurance Unmanned Underwater Vehicle Systems

Justin T. Kleiber

Dissertation submitted to the Faculty of the
Virginia Polytechnic Institute and State University
in partial fulfillment of the requirements for the degree of

Master of Science
in
Computer Engineering

Daniel J. Stilwell, Chair
Thinh T. Doan
Ryan K. Williams

May 2, 2022
Blacksburg, Virginia

Keywords: Autonomous Underwater Vehicles, Robust Control, Gaussian Processes

Control Design for Long Endurance Unmanned Underwater Vehicle Systems

Justin T. Kleiber

(ABSTRACT)

In this thesis we demonstrate a technique for robust controller design for an autonomous underwater vehicle (AUV) that explicitly handles the trade-off between reference tracking, agility, and energy efficient performance. AUVs have many sources of modeling uncertainty that impact the uncertainty in maneuvering performance. A robust control design process is proposed to handle these uncertainties while meeting control system performance objectives. We investigate the relationships between linear system design parameters and the control performance of our vehicle in order to inform an $\mathcal{H}_\infty$ controller synthesis problem with the objective of balancing these tradeoffs. We evaluate the controller based on its reference tracking performance, agility and energy efficiency, and show the efficacy of our control design strategy.

Control Design for Long Endurance Unmanned Underwater Vehicle Systems

Justin T. Kleiber

(GENERAL AUDIENCE ABSTRACT)

In this thesis we demonstrate a technique for autopilot design for an autonomous underwater vehicle (AUV) that explicitly handles the trade-off between three performance metrics. Mathematical models of AUVs are often unable to fully describe their many physical properties. The discrepancies between the mathematical model and reality impact how certain we can be about an AUV's behavior. Robust controllers are a class of controller that are designed to handle uncertainty. A robust control design process is proposed to handle these uncertainties while meeting vehicle performance objectives. We investigate the relationships between design parameters and the performance of our vehicle. We then use this relationship to inform the design of a controller. We evaluate this controller based on its energy efficiency, agility and ability to stay on course, and thus show the effectiveness of our control design strategy.

Dedication

For my wife Andrea

Acknowledgments

First, I would like to express my gratitude to my family for supporting me every step of the way through my Master's degree. I would not be where I am today without them. I also want to thank my wife Andrea, to whom this thesis is dedicated. Without her love and support, it would have been impossible for me to succeed. This thesis reflects two years of research in the Center for Marine Autonomy and Robotics at Virginia Tech, and in that time period I have worked with some great teammates and advisors. I would like to thank Dr. Stilwell for providing me with this opportunity, while also guiding me in every aspect of this thesis. I am grateful for my fellow lab members Conlan Edwards, Benjamin Biggs, Hans He, Charles Watson and Stephen Krauss. The help I've received from them in the lab and in classes has been greatly appreciated, but their friendship has been even more vital for me. I would also like to thank my fellow co-authors Dr. Stefano Brizzolara and Lakshmi Miller for helping with the hydrodynamic modeling and with their advice on the wing analysis demonstrated in this thesis. I am thankful for Dr. Ryan Williams and Dr. Thinh Doan, for being supportive of this research and for the time they have taken to provide oversight on this project in their service on my committee. Finally, I thank whoever is reading this for finding my work interesting. I hope you find what you are looking for.

Contents

List of Figures **ix**

List of Tables **xii**

1 Introduction **1**

2 Uncertain Vehicle Dynamics **2**

2.1 Introduction 2

2.2 Gaussian Process Regression 4

2.3 Coefficient Selection 5

2.4 Coefficient Relationship to Performance 7

2.5 Experimental Results 9

2.5.1 Single Coefficient Analysis 9

2.5.2 Paired Coefficient Analysis 13

2.6 Conclusion 14

3 Effect of Wing Design on Endurance of Long-Range AUVs **17**

3.1 Introduction 17

3.2 Wing Modeling 18

3.2.1 Wing Dynamics 18

3.2.2 Wing Parameter Selection 21

3.3 Design Optimization Problem 23

3.3.1 Wingless AUV 24

3.3.2 AUV with a Wing 26

3.4 Results 27

3.4.1 690 AUV 27

3.4.2 DIVE-LD UUV 29

3.5 Conclusions 30

4 Controller Design and Evaluation **32**

4.1 Introduction 32

4.2 Performance Metrics 33

4.2.1 AUV Dynamics 34

4.2.2 Control Energy Cost 34

4.2.3 Tracking Error 39

4.2.4 Agility 39

4.3 Modeling Characteristics 40

4.3.1 Actuator Disturbance 40

4.3.2 Loop Shaping Functions 41

4.4 Sensitivity Relationship to Performance 44

4.5 $\mathcal{H}_\infty$ Control Design 46

4.6 Experimental Results 51

5 Conclusions **53**

Bibliography **54**

Appendices **59**

Appendix A Full Uncertainty Mappings **60**

Appendix B Performance Variance Tables **66**

List of Figures

2.1 The 690 AUV developed at Virginia Tech. Photo courtesy of Conlan Edwards 5

2.2 Relationship between variances of $N_{uu\delta}$ and yaw rate settling time 10

2.3 A GP is used to estimate a functional relationship on data in Fig. 2.2 11

2.4 Relationship between variances of $Y_{\dot{v}}$ and settling time 11

2.5 A GP estimates the relationship shown in Fig. 2.4 12

2.6 Relationship between the variances of Y_{ur}, $Y_{uu\delta}$ and % Overshoot variance . 16

2.7 A GP is used to estimate the relationship shown in Fig. 2.6 16

3.1 Relationship between Reynolds number and $C_{l\alpha}$ 23

3.2 Relationship between Reynolds number and C_{D_0} 24

3.3 Comparison between nominal 690 AUV and optimal static wing configurations at 2 m/s with different buoyancies 28

3.4 Comparison between nominal 690 AUV and optimal static wing configurations at 1.5 m/s with different buoyancies 29

3.5 Comparison between nominal DIVE-LD UUV and optimal static wing configurations at 3 m/s with different buoyancies 30

3.6 Comparison between nominal DIVE-LD UUV and optimal static wing configurations at 2 m/s with different buoyancies 31

4.1 Servo block diagram 35

4.2 Armature servo circuit 36

4.3 Current, angle, and armature voltage trajectory for the servo motor 38

4.4 Effect of different values for K_d on peak to peak error in simulated pitch . . 41

4.5 Simulated pitch error at $K_d = 1, 2, 3$ 42

4.6 Field data with a PID autopilot shows about ±0.2 degrees of peak to peak oscillations in pitch error 43

4.7 Multi Input Multi Output Feedback System 43

4.8 Performance vs peak sensitivity. Energy use can be reduced with only a small performance reduction 45

4.9 Performance tradeoffs for peak complementary sensitivity 45

4.10 AUV pitch axis system diagram 46

4.11 Unweighted $\mathcal{H}_\infty$ model for the AUV pitch control problem. 47

4.12 Weighted $\mathcal{H}_\infty$ model for the AUV pitch control problem. 48

4.13 Performance tradeoffs for various choices of gain W_g for W_1 at $K_d = 1.5$ disturbance gain 51

4.14 Nonlinear simulation trajectory for pitch error with $W_g = 5$ at $K_d = 1.5$ actuator disturbance gain 52

A.1 Rise time variance vs coefficient variance for each coefficient 60

A.2 A GP estimates the rise time variance vs coefficient variance for each coefficient 61

A.3 Settling time variance vs coefficient variance for each coefficient 62

A.4 A GP estimates the settling time variance vs coefficient variance for each coefficient 63

A.5 % overshoot variance vs coefficient variance for each coefficient 64

A.6 A GP estimates the % overshoot variance vs coefficient variance for each coefficient 65

List of Tables

2.1 Estimated values and variances for each coefficient of interest. 7

2.2 Impact of each coefficient's variance on rise time variance 13

2.3 Impact of each coefficient's variance on settling time variance 14

2.4 Impact of each coefficient's variance on % overshoot variance 15

3.1 690 AUV hydrodynamic coefficients 25

3.2 DIVE-LD UUV hydrodynamic coefficients 26

4.1 Futaba BLS137SV servo motor characteristics [2] 37

4.2 Servo Coefficient Estimates 38

B.1 Impact of joint coefficient uncertainties on rise time uncertainty 66

B.2 Impact of joint coefficient uncertainties on settling time uncertainty 67

B.3 Impact of joint coefficient uncertainties on % overshoot uncertainty 68

List of Abbreviations

AUV	Autonomous underwater vehicle
CB	Center of buoyancy
CFD	Computational fluid dynamics
EMPC	Economic model predictive control
GP	Gaussian process
MIMO	Multi-input multi-output
NACA	National Advisory Committee for Aeronautics
PID	Proportional integral derivative
RMS	Root mean square
RPM	Revolutions per minute
UAV	Unmanned aerial vehicle
UUV	Unmanned underwater vehicle
VPMM	Virtual planar motion mechanism

Chapter 1

Introduction

Autonomous underwater vehicles (AUVs) are nonlinear dynamical systems that are challenging to model accurately. Dynamic models of an AUV may have various sources of uncertainty that must be accounted for in control design. In particular, estimating each hydrodynamic coefficient for a nonlinear AUV model has a level of uncertainty, and each coefficient has a different impact on the maneuvering performance of the vehicle. This thesis presents the effect of modeling uncertainty on the uncertainty in maneuvering performance as a motivation for robust control design.

AUV missions can cover large areas in demanding environments and be long in duration. Therefore, AUV control systems must have low reference tracking error throughout the mission. AUVs often operate in areas with rapid changes in terrain, which requires a vehicle to be agile. Additionally, vehicle endurance must be considered in the controller design process. A wing design procedure is performed to investigate the tradeoffs of adding a wing to a long-range AUV. The influence of loop-shaping design choices on the tradeoff between agility, tracking error and energy cost to maintain steady state is explored. These findings allow us to develop loop-shaping design goals for a controller.

Robust controllers are designed to achieve performance guarantees for a system under some uncertainty. We use the relationship between loop-shaping design choices and vehicle performance to synthesize an $\mathcal{H}_\infty$ controller for the pitch control of an AUV. The experimental results for this controller are evaluated in Chapter 4.

Chapter 2

Uncertain Vehicle Dynamics

This chapter is adapted from the conference paper *Assessing the Effect of Hydrodynamic Parameter Uncertainty on AUV Performance with Gaussian Processes* by Justin Kleiber, Lakshmi Miller, Stephen Krauss, Daniel Stilwell and Stefano Brizzolara [16].

2.1 Introduction

We seek a method for assessing how the uncertainty in hydrodynamic coefficients leads to uncertainty in the maneuvering predictions for an autonomous underwater vehicle (AUV). For example, uncertainty in various hydrodynamic coefficients leads to various levels of uncertainty in how much overshoot an AUV exhibits while transitioning to a desired depth. Improved methods for predicting uncertainty in AUV performance may help identify specific coefficients that need to be the most accurately measured and, furthermore, determine what accuracy is required to get a meaningful prediction. This would enable control design that is robust to specific coefficient uncertainties rather than to general overall modeling uncertainty, yielding more robustness and better performance [17][25].

Prior work in AUV modeling analyzes the sensitivity of underwater vehicles to coefficient values by systematically varying coefficients and recording the performance [23]. This method has also been used on surface vessels [30]. While these approaches express the impact a coefficient has on system performance, they do not address uncertainty in the hydrodynamic coefficients. Additionally, the sensitivity analysis presented in these works is not intended to gain an understanding of the sensitivity of the system's performance to multiple coefficients at once.

Gaussian processes (GPs) are a Bayesian approach to estimating an unknown function that is well suited for modeling uncertainty. GPs have been proven to be a powerful tool in regression analysis, and offer a Bayesian alternative to neural networks [33]. Additionally, GPs have been used in system identification of fixed-wing unmanned aerial vehicles (UAVs) to estimate varying aerodynamic coefficients during flight [14]. By using the variance of the GP solution, the results demonstrate how using GPs can indicate the confidence in the system identification prediction in addition to providing an accurate estimate. Other work has used the ability of GPs to model prediction uncertainty to deploy them as metamodels in design optimization problems, where the GP quantifies how uncertainty in inputs impacts uncertainty in a design's performance [29].

In this chapter, a GP model is first used to find sensitivity of the system to the coefficients that populate a non-linear lumped-parameters dynamic model [21] obtained by high fidelity unsteady CFD simulations on an underwater autonomous vehicle designed and built at Virginia Tech's Center for Marine Autonomy and Robotics. This GP is leveraged to understand performance uncertainty given modeling uncertainty by using a Monte-Carlo approach for approximating the variance of the performance distribution. Use of a GP to model uncertainty allows us to rigorously keep track of the correlation between uncertain vehicle hydrodynamic coefficients and measures of AUV performance, which is a significant contribution of our work.

2.2 Gaussian Process Regression

We can take a GP to be a distribution over functions as in [27]. For some unknown function $f(x)$, we have a GP composed of a mean and covariance function

$$m(x) = \mathbb{E}[f(x)] \tag{2.1}$$

$$k(x, x^*) = \mathbb{E}[(f(x) - m(x))(f(x^*) - m(x^*))] \tag{2.2}$$

and we have that the function $f(x)$ is estimated by the GP such that

$$f(x) \sim \mathcal{GP}(m(x), k(x, x^*)) \tag{2.3}$$

A GP is trained using a set $\mathcal{G} = \{(x, v) \mid x \in D, v \in V\}$, consisting of a set of independent variables D and a corresponding set of measurements, V. In our work, the independent variables are hydrodynamic coefficients, and the measurements are AUV performance metrics. Given an input $x \in D$, we have an unknown function f that maps x to a Gaussian distribution.

We say that a GP is a probability distribution for the unknown function f. The mean and variance of the function at a given $x \in D$ is $\mu(x)$ and $\sigma^2(x)$ respectively. Indeed, the distribution of f at x is Gaussian. That is, given the training data $\mathcal{G}$,

$$p(f(x)|x, D) \sim \mathcal{N}(\mu(x), \sigma^2(x)) \tag{2.4}$$

Because the actual hydrodynamic coefficients are uncertain, we consider the case that x_q are realizations of a Gaussian distribution $p_q(x_q)$, and we follow the process in [13] to compute the corresponding predictive distribution. That is, given training data $\mathcal{G}$,

$$p(f(x_q)|\mathcal{G}) = \int p(f(x_q), x_q|\mathcal{G})dx \tag{2.5}$$

$$= \int p(f(x_q)|x_q, \mathcal{G})p_q(x_q)dx \tag{2.6}$$

Then (2.6) is approximated at $x_q = x^*$ by

$$\frac{1}{T}\sum_{i=1}^{T} p(f(x^*)|x_i, D) \tag{2.7}$$

where $x_i{}_i^T$ are a set of T independent samples drawn from $p_q(x_q)$.

2.3 Coefficient Selection

Figure 2.1: The 690 AUV developed at Virginia Tech. Photo courtesy of Conlan Edwards

The 690 AUV developed at Virginia Tech is the vehicle used to illustrate the results of the analysis, and is shown in Figure 2.1. From [22] we have the dynamics of the 690 AUV to be

$$\dot{\nu} = f(\nu, u) = M^{-1}\left(C_a\nu - C_{rb}\nu + D\nu + G + \tau\right) \tag{2.8}$$

In this chapter we consider only the dynamics from [21] which represent the yaw-axis motion. Thus, $\nu = [u, v, r]^\intercal$ and u, v, r are the surge velocity, sway velocity and yaw rate respectively. The analysis in this chapter focuses on hydrodynamic coefficients that appear to have the greatest effect on the horizontal plane maneuvering as seen in a numerical model for the 690 AUV. We consider nominal operating conditions corresponding to level flight at 2 m/s. The nonlinear dynamical system is linearized around the operating point with nominal rudder angle, $\delta_r^* = 0$.

$$\dot{\nu} = \left.\frac{\partial f}{\partial \nu}\right|_{\nu^*}(\nu - \nu^*) + \left.\frac{\partial f}{\partial \delta_r}\right|_{\delta_r^*}\delta_r \tag{2.9}$$

The terms that appear in this linearized model have coefficients $N_{\dot{r}}$, N_{ur}, $N_{uu\delta}$, N_{uv}, $N_{\dot{v}}$, $Y_{\dot{r}}$, Y_{ur}, Y_{uv}, $Y_{uu\delta}$, and $Y_{\dot{v}}$. We assume that the 690 AUV horizontal plane dynamics are significantly impacted by these terms.

Nominal values for each hydrodynamic coefficient of the 690 AUV are estimated using custom numerical models built on StarCCM+ v13.04.11, which is a high fidelity general purpose computational fluid dynamics (CFD) unsteady Reynolds averaged Navier Stokes equation (RANSE) solver. StarCCM+ was used to simulate pure-sway virtual planar motion mechanism (VPMM) maneuvers and steady drift yaw angle towing tests [21] [7] [15]. These coefficient estimates are computed from a least-squares fit of forces and moments generated by the CFD tool. The variance of an estimate is produced from the regressive weight of steady drift data to refine the VPMM sway coefficients, as shown in [21], and from the magnitude of hull drift angles used to obtain steady drift data. The value and variance for each of the hydrodynamic coefficients of interest for the 690 AUV are shown in Table 2.1.

	Value	Variance
$N_{\dot{r}}$	-14.5316	0.0014996
N_{ur}	-24.2459	0.21863
$N_{uu\delta}$	-9.1827	0.472
N_{uv}	-11.4956	1.6921
$N_{\dot{v}}$	3.67491	3.8301e-07
$Y_{\dot{r}}$	2.6899	0.016527
Y_{ur}	23.6598	0.36356
Y_{uv}	-34.5946	0.59138
$Y_{uu\delta}$	9.0728	0.759
$Y_{\dot{v}}$	-48.238	2.1591e-08

Table 2.1: Estimated values and variances for each coefficient of interest.

2.4 Coefficient Relationship to Performance

In this section, we briefly describe our method for parameterizing the mapping between hydrodynamic coefficient uncertainty and AUV performance uncertainty. For each coefficient of interest, we take 20 linearly spaced values from an interval that is ±50% about the nominal coefficient value in Table 2.1, and for each value simulate the AUV horizontal plane dynamics on a 10 degree rudder step input. We compute three maneuvering performance metrics for yaw rate: rise time, settling time, and overshoot.

For a given coefficient, the input set D consists of 20 linearly spaced values, and the measurement set V consists of the corresponding performance values obtained via simulation. Thus, the training set is the tuple $\mathcal{G} = \{(x, y) \mid x \in D, y \in V\}$. Using the Monte-Carlo strategy from (2.7), we then take T samples of a hydrodynamic coefficient from a normal distribution with a prescribed variance and the nominal coefficient value as the mean. Using the GP trained on $\mathcal{G}$, the performance variance, σ_p^2, is estimated using (2.4) and (2.7). Repeating this for a set of coefficient variances is used to compute a mapping from coefficient variance to performance metric variance, as outlined in Algorithm 1.

Algorithm 1 Variance Mapping Algorithm

Input: A GP, $f(\cdot)$ for the coefficient and performance metric of interest, the coefficient's mean, μ, a set of variances to test H, and the sample size T.

Output: A set of the resulting performance variances, P.

```
procedure MAP_VARIANCE($f(\cdot)$, $\mu$, $H$, $T$)
    $P \leftarrow \{\}$;
    for $\sigma_q^2 \in H$ do
        $X \leftarrow$ Sample $T$ values, $x \sim \mathcal{N}(\mu, \sigma_q^2)$;
        $\sigma_p^2 \leftarrow 0$;
        for $x \in X$ do
            $\sigma_p^2 \leftarrow \sigma_p^2 + \frac{1}{T} Var[f(x)]$ (2.4),(2.7);
        end for
        $P \leftarrow P \cup \{\sigma_p^2\}$;
    end for
    return $P$;
end procedure
```

A benefit of a GP model is that covariance between coefficients is explicitly addressed, which allows us to model how uncertainty of multiple hydrodynamic coefficients affects uncertainty in performance. To find how combinations of coefficients affect maneuvering performance, we repeat the univariate uncertainty analysis in a multivariate setting. Taking two coefficients at a time, the intervals chosen in the univariate case are used to create a set of inputs D_1, D_2 for each coefficient. We take these sets to form the set of coefficient combinations to test, $D = D_1 \times D_2$. The system is simulated for each $(x_1, x_2) \in D$ to find the performance outputs

V. A GP is computed that estimates the relationship between these two coefficient values and the corresponding performance outputs. Algorithm 1 is extended to find the variance mapping for the paired coefficients case by taking two variance distributions and testing the combination of coefficient variances to find a relationship between multivariate coefficient uncertainty and performance uncertainty. This process is shown in Algorithm 2.

Algorithm 2 Paired Coefficient Variance Mapping Algorithm

Input: A GP, $f(\cdot)$ for the coefficients and performance metric of interest, the coefficient means, μ_1, μ_2, sets variances to test H_1, H_2, and the sample size T.
Output: A set of the resulting performance variances, P.

```
procedure MAP_PAIRED_VARIANCE($f(\cdot)$, $\mu_1$, $\mu_2$, $H_1$, $H_2$, $T$)
    $P \leftarrow \{\}$;
    for $\sigma_1^2 \in H_1$ do
        for $\sigma_2^2 \in H_2$ do
            $X \leftarrow$ Sample $T$ values, $x \sim \mathcal{N}(\mu, \sigma_1^2)$;
            $Y \leftarrow$ Sample $T$ values, $y \sim \mathcal{N}(\mu, \sigma_2^2)$;
            $\sigma_p^2 \leftarrow 0$;
            for $(x, y) \in (X, Y)$ do
                $\sigma_p^2 \leftarrow \sigma_p^2 + \frac{1}{T} Var[f(x, y)]$ (2.4),(2.7);
            end for
            $P \leftarrow P \cup \{\sigma_p^2\}$;
        end for
    end for
    return $P$;
end procedure
```

2.5 Experimental Results

2.5.1 Single Coefficient Analysis

In the univariate analysis, fifty values linearly spaced between 0 and 100 were chosen as the set of variances to investigate for each coefficient. The Monte-Carlo sample size, $T = 400$, is chosen for the uncertain coefficient inputs to the GP. The GP uses a squared exponential covariance function with isotropic distance measure and a Gaussian likelihood function. The hyperparameters of the GP are found using the GPML toolbox in MATLAB [26]. Algorithm 1 is used to relate a given coefficient's uncertainty to performance uncertainty.

As an example, $N_{uu\delta}$ had a notable impact on the variance of settling time, as shown in Figure 2.2. To estimate the variance between each of the 50 sample points, an additional GP was trained on these results to find a functional relationship. The result of the GP training on the relationship between $N_{uu\delta}$ and settling time is shown in Figure 2.3. The gray band in Figure 2.3 represents the 95% confidence interval in the GP regression prediction that maps coefficient variance to performance variance.

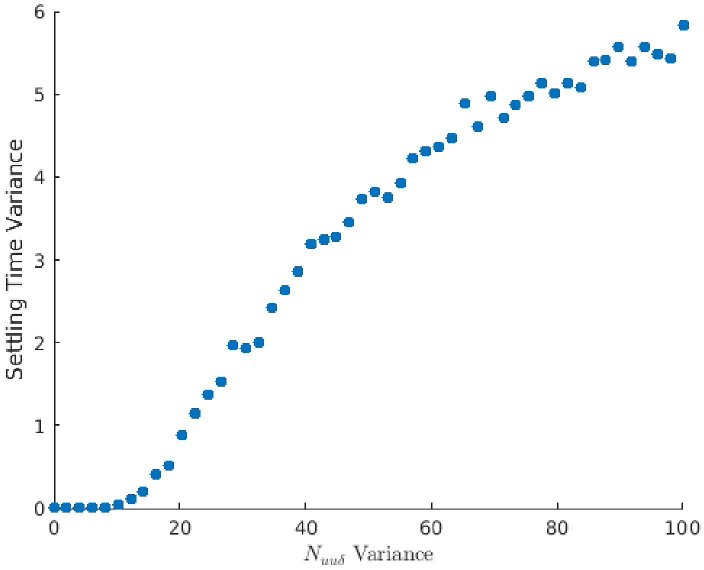

Figure 2.2: Relationship between variances of $N_{uu\delta}$ and yaw rate settling time

However, not all coefficients have such a large impact on performance uncertainty at higher estimation variances. As shown in Figure 2.4, the uncertainty of coefficient $Y_{\dot{v}}$ has very little effect on the uncertainty of the settling time of the AUV. The corresponding GP for this coefficient is shown in Figure 2.5. Similar plots for all combinations of hydrodynamic coefficient and performance metric are shown in Appendix A.

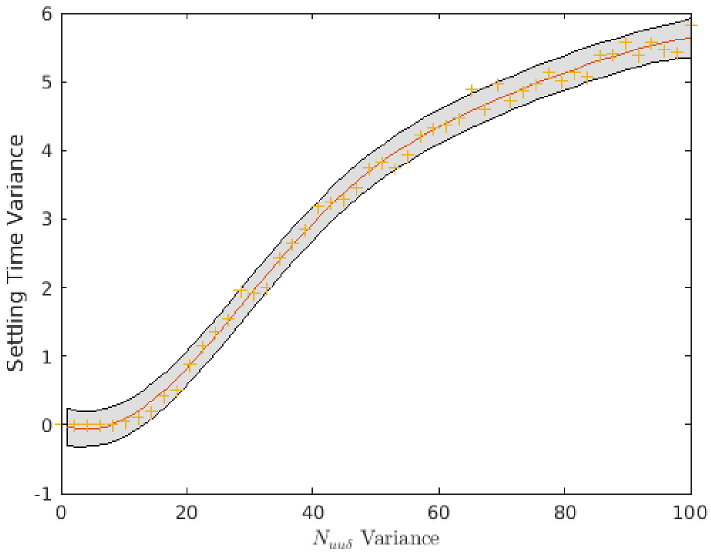

Figure 2.3: A GP is used to estimate a functional relationship on data in Fig. 2.2

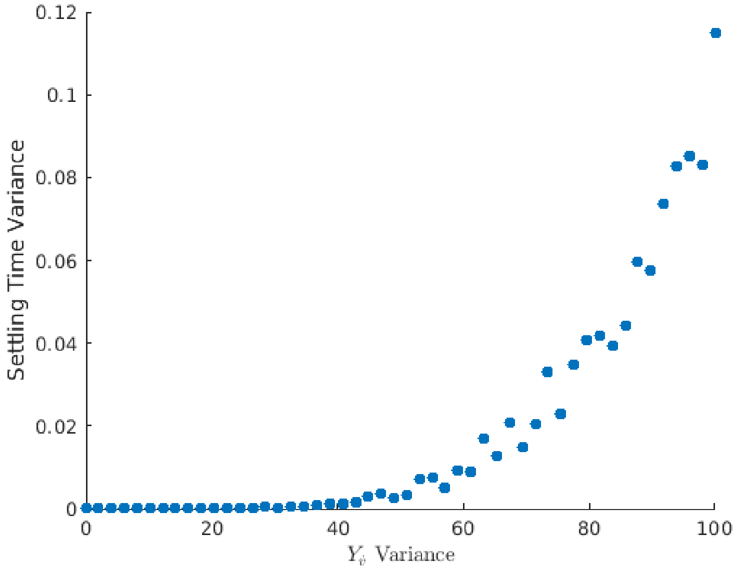

Figure 2.4: Relationship between variances of $Y_{\dot{v}}$ and settling time

Graphical analysis using GPs shows how performance uncertainty evolves with respect to measurement uncertainty for a given coefficient. Given maneuvering performance uncertainty tolerances, this can be used to estimate the level of coefficient measurement uncer-

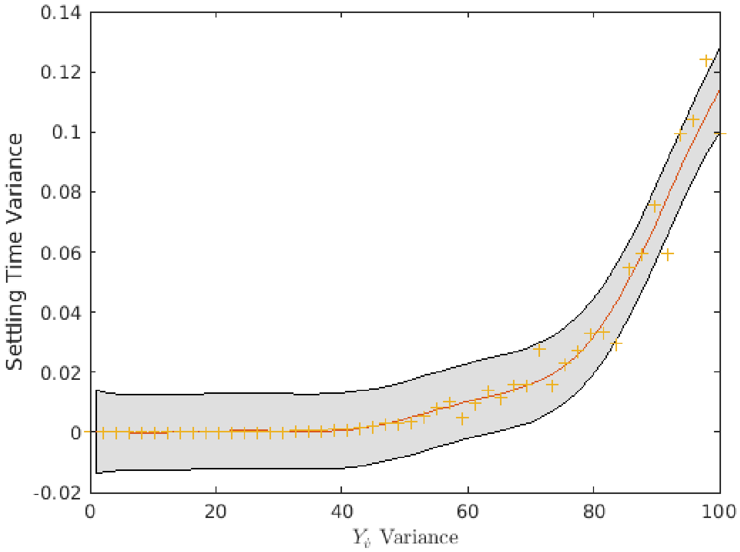

Figure 2.5: A GP estimates the relationship shown in Fig. 2.4

tainty that is acceptable. Additionally, with prior knowledge of the coefficient variance from the CFD/VPMM estimation procedure, we can leverage the GPs to find a point estimate of the impact each coefficient's uncertainty has on performance uncertainty of our design model. To make such a point estimate for a given coefficient, we take the corresponding coefficient variance from Table 2.1 and construct H to be a single element set containing this variance. We pass H as the input to Algorithm 1. Repeating the process for each coefficient, we compute the effect each coefficient's uncertainty has on the uncertainty for each performance metric, as shown in Table 2.2, 2.3, and 2.4.

From the point estimates in Table 2.2, 2.3, and 2.4, we can see that while the estimation variance of $N_{\dot{r}}$ is low in the 690 AUV model, it has the largest impact of any coefficient on settling time variance. Similarly, this analysis reveals that while N_{uv} has the highest estimated variance of all coefficients of interest in the model, N_{uv} only appears to have the greatest impact of all coefficients with respect to the variance in percent overshoot. The higher estimation variance of N_{uv} contributes less to performance variance relative to other

	Rise Time Variance (sec^2)
$N_{\dot{r}}$	7.8228e-06
N_{ur}	5.4475e-06
$N_{uu\delta}$	7.4982e-07
N_{uv}	4.5809e-06
$N_{\dot{v}}$	3.5733e-06
$Y_{\dot{r}}$	1.1918e-06
Y_{ur}	5.2621e-06
Y_{uv}	5.4922e-06
$Y_{uu\delta}$	1.0163e-06
$Y_{\dot{v}}$	2.5504e-06

Table 2.2: Impact of each coefficient's variance on rise time variance

coefficients in the other two metrics.

2.5.2 Paired Coefficient Analysis

In the multivariate case, every combination of two coefficients was analyzed. Fifty linear spaced values between 0 and 100 were chosen for each coefficient's variance set. The Monte-Carlo sample size for each of the two uncertain coefficient distributions was chosen to be $T = 400$. Algorithm 2 is used to relate the joint uncertainty of two hydrodynamic coefficients to performance uncertainty.

As an example, the variances of Y_{ur} and $Y_{uu\delta}$ jointly affect the rise time of the system, as shown in Figure 2.6. Like in the univariate case, a GP is used to estimate the relationship between the two coefficient variances and the overshoot variance. The fit of this GP to the data is shown in Figure 2.7.

	Settling Time Variance (sec^2)
$N_{\dot{r}}$	0.00019563
N_{ur}	0.00011753
$N_{uu\delta}$	1.4583e-05
N_{uv}	0.00012638
$N_{\dot{v}}$	7.6586e-05
$Y_{\dot{r}}$	4.3121e-05
Y_{ur}	0.00016794
Y_{uv}	0.00014816
$Y_{uu\delta}$	3.1532e-05
$Y_{\dot{v}}$	7.0791e-05

Table 2.3: Impact of each coefficient's variance on settling time variance

The graphical output of the paired coefficient analysis reveals how uncertainties contribute to performance uncertainty in a coupled manner. To understand how this applies to pairs of coefficients from the 690 AUV design model, we take the known variances from Table 2.1 and use every combination of coefficient variances to iteratively construct the single element sets H_1 and H_2, which are used as inputs to Algorithm 2. With this process, we find the effect of pairwise uncertainties on the uncertainty for rise time, settling time, and overshoot respectively, as shown in Table B.1, B.2 and B.3.

2.6 Conclusion

In this chapter, GPs are used to estimate the relationship between uncertainty in hydrodynamic coefficients and the uncertainty in the maneuvering performance prediction of an AUV using a lumped-parameters model. The process of selecting dominant terms from the

	% Overshoot Variance ($\%^2$)
$N_{\dot{r}}$	5.6326e-06
N_{ur}	1.511e-05
$N_{uu\delta}$	2.5346e-05
N_{uv}	0.00040772
$N_{\dot{v}}$	3.6971e-06
$Y_{\dot{r}}$	1.784e-06
Y_{ur}	4.8437e-06
Y_{uv}	0.00028495
$Y_{uu\delta}$	9.2303e-05
$Y_{\dot{v}}$	1.6758e-05

Table 2.4: Impact of each coefficient's variance on % overshoot variance

nonlinear model is shown, and the relationship between vehicle performance and these terms is investigated. Analysis is carried out using a GP to determine how individual coefficient uncertainties affect maneuvering performance uncertainty. An additional GP is used to represent the relationship between coefficient uncertainty and maneuvering performance uncertainty. Examples of a high-impact coefficient and a low impact coefficient are used to highlight the effectiveness of using GPs in the single coefficient analysis to visualize the effect of coefficient measurement uncertainty on performance uncertainty. The proposed method can be used to show the impact of each coefficient on the uncertainty of each performance metric. The analysis is then extended to the multivariate setting to show the ability of the procedure to relate joint coefficient uncertainties to performance uncertainty, and the GP regression is demonstrated to work in the multivariate approach.

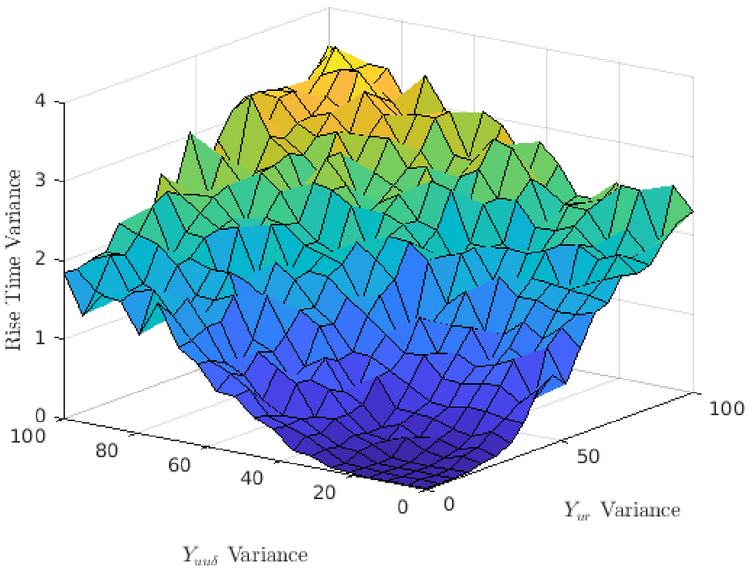

Figure 2.6: Relationship between the variances of Y_{ur}, $Y_{uu\delta}$ and % Overshoot variance

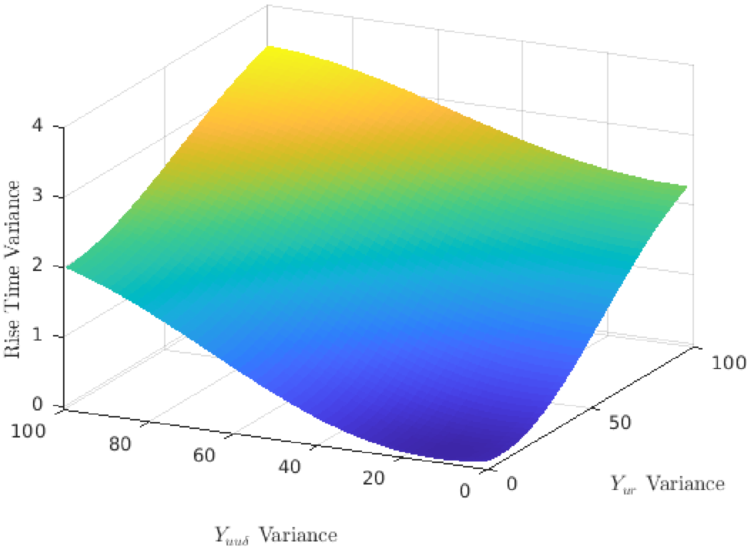

Figure 2.7: A GP is used to estimate the relationship shown in Fig. 2.6

Chapter 3

Effect of Wing Design on Endurance of Long-Range AUVs

3.1 Introduction

For long range autonomous underwater vehicles (AUVs), the thruster that propels the vehicle is a large factor in the consideration of the vehicle's range. The primary contribution of this chapter is the development of a procedure to identify wing design specifications that minimize thrust required at an equilibrium point for an autonomous underwater vehicle. This is motivated by the hypothesis that a wing might reduce overall drag in certain operating conditions. When buoyancy is nonzero, the AUV body must generate lift to remain at a constant depth. The AUV body can generate lift when the body has a nonzero angle of attack, but at the expense of additional drag. A wing attached to the body will also generate lift, but with a higher lift-to-drag ratio than the body. For the same net lift generated by the wing and the body, we seek to identify operating conditions where the angle of attack is smaller than for the body alone, and for which the net drag from the body and the wing is reduced.

In [6], a variable buoyancy engine is used to keep a long-range AUV neutrally buoyant throughout a mission. This approach reduces drag on the vehicle body, but is typically expensive in terms of volume. This motivates the design of a wing, which may be more simple to add to an existing AUV.

For slow moving vehicles, wings can generate lift more efficiently than the hull [10]. Follow on work in [11] illustrated a wing design for the concept design in [10]. Recent work on a later iteration of that particular vehicle has shown that a wing can be designed as a passive method for generating downforce for a long range AUV that has a maximum depth of 6000 meters, and a mission range of 1800 kilometers [28]. However, the design space for the wing is not fully explored and the benefit of the wing to vehicle endurance is not investigated.

In this chapter, we assess the ability of a wing to reduce drag during steady horizontal motion for various speeds and buoyancy conditions. We solve an optimization problem that seeks to identify minimum-thrust equilibrium conditions, which is equivalent to minimizing drag, and therefore maximizing endurance. We consider two different AUVs. For each AUV, we compare the nominal, wingless configuration to configurations of the vehicle with a wing added between its stern and center of buoyancy (CB) to assess the benefit of adding a wing.

3.2 Wing Modeling

3.2.1 Wing Dynamics

To assess the potential benefit of adding a wing to a long range AUV, the design space of including a rectangular NACA-0012 wing is explored. To consider a wing for an AUV, (2.8) is modified by adding τ_{wing}, the forces and moments associated with an added wing

$$\dot{\nu} = f(\nu, u) = M^{-1}\left(C_a\nu - C_{rb}\nu + D\nu + G + \tau + \tau_{wing}\right) \tag{3.1}$$

where $\nu = [u, v, w, p, q, r]^\intercal$ and u, v, w are the surge velocity, sway velocity and heave velocity respectively, while p, q, r are the roll rate, pitch rate and yaw rate respectively. We define

$$\tau_{wing} = \begin{bmatrix} \tau_u & 0 & \tau_w & 0 & \tau_q & 0 \end{bmatrix}^\intercal \tag{3.2}$$

where τ_u is the body relative drag in the surge axis, τ_w is the body relative lift in the heave axis, and τ_q is the pitch moment induced by the wing. The wings are symmetric, which allows the assumption that they act only in the vertical plane. From this modification, the dynamics for this analysis can be simplified to only include the pitch axis plane for which the state of the AUV is expressed $\nu = [u, w, q]^\intercal$.

From (1.1) in [4], the total lift from the wing is

$$L = \frac{1}{2}\rho v^2 S C_L \tag{3.3}$$

where ρ is the density of water, v is the velocity, S is the planform area and C_L is a linear approximation of the lift coefficient defined as

$$C_L = C_{L\alpha}\alpha \tag{3.4}$$

where α is the angle of attack for the wing given the vehicle angle of attack and wing deflection, and $C_{L\alpha}$ is the slope of the relationship between C_L and α adjusted for a three-dimensional wing with a finite aspect ratio as in [32]

$$C_{L\alpha} = C_{l\alpha} AR \frac{AR + 0.7}{(AR + 1.7)^2} \tag{3.5}$$

where $C_{l\alpha}$ is the slope of the relationship assuming an infinite aspect ratio, and AR is the aspect ratio of the wing defined as

$$AR = \frac{S}{c} \tag{3.6}$$

where S and c are span and chord of the wing respectively. Since there are two symmetric identical wings, the lift, L, is doubled, yielding

$$L = \rho v^2 S C_L \tag{3.7}$$

From (1.2) in [4] the total drag from the wing is

$$D = \frac{1}{2}\rho v^2 S C_D \tag{3.8}$$

where C_D is the drag coefficient defined as

$$C_D = C_{D_0} + \frac{C_L^2}{\pi e_0 AR} \tag{3.9}$$

where C_{D_0} is the drag coefficient at zero lift, e_0 is the Oswald efficiency number (which is 0.7 for rectangular wings [3]). As with lift, since there are two symmetric identical wings the drag, D, is doubled, yielding

$$D = \rho v^2 S C_D \tag{3.10}$$

The lift force generated by the wing applies perpendicular to the wing's angle of attack. Furthermore, the drag force induced by the wing applies parallel to the angle of attack. Neither force applies directly in the body reference frame, and must be rotated to apply correctly. Thus, (3.7) and (3.10) are rotated into the body frame by

$$\tau_u = L \sin\alpha - D \cos\alpha \tag{3.11}$$

$$\tau_w = L \cos\alpha - D \sin\alpha \tag{3.12}$$

With the vertical force generated in the body reference frame, τ_w, the pitch moment τ_q is computed

$$\tau_q = -\tau_w \ell \tag{3.13}$$

where ℓ is the wing location with respect to the center of buoyancy of the AUV. A positive value for ℓ indicates a wing forward of the center of buoyancy, while a negative value for ℓ indicates a wing toward the rear. The negative sign on the right hand side of the equation is used to preserve the sign convention from [22] where positive τ_w indicates downward motion, while positive τ_q indicates an upward pitch moment.

3.2.2 Wing Parameter Selection

In the following analysis, the design space of the wing is parameterized by span, chord, wing location, and wing deflection angle. However, the lift and drag properties of the wing vary with the Reynolds number associated with the design parameters. The equation for Reynolds number is

$$Re = \frac{\rho v L}{\mu} \tag{3.14}$$

where ρ is the density of the fluid in kg/m^3, v is the flow velocity, L is the characteristic length in meters, and μ is the dynamic viscosity of the fluid in Pa-s. For our analysis, we take the wing chord length to be the characteristic length, $\rho = 1000$ kg/m^3, and $\mu = 1.002 \times 10^{-3}$ Pa-s for water at 20 degrees Celsius [31].

For constant flow velocity, chord length and temperature, the Reynolds number is constant. With a constant Reynolds number, the $C_{l\alpha}$ and C_{D_0} coefficients are chosen readily from an airfoil database such as [1] for the NACA-0012 airfoil.

For our analysis we assume a constant temperature and flow velocity, however the chord length changes based on the wing design. In exploring the design space, the minimum chord length may be up to three times smaller than the maximum chord length, resulting in large changes to the Reynolds number. As shown in Figures 3.1 and 3.2, large changes in Reynolds number may result in small changes to a wing's lift and drag coefficients, however, these changes are large enough to affect the analysis. This motivates an automatic way of determining a wing's lift and drag coefficients based on a variable Reynolds number. Given the linear mapping between Reynolds number and $C_{l\alpha}$

$$C_{l\alpha} = \beta_1 Re + \beta_0 \tag{3.15}$$

we use least squares regression to find the optimal coefficients

$$\begin{aligned} \beta_0 &= 0.109 \\ \beta_1 &= 9.67 \times 10^{-9} \end{aligned} \tag{3.16}$$

The results of this regression are shown in Figure 3.1.

A power regression is performed to find a mapping between Reynolds number and C_{D_0}, resulting in

$$C_{D_0} = 4.19 Re^{-0.488} \tag{3.17}$$

This relationship is shown in Figure 3.2.

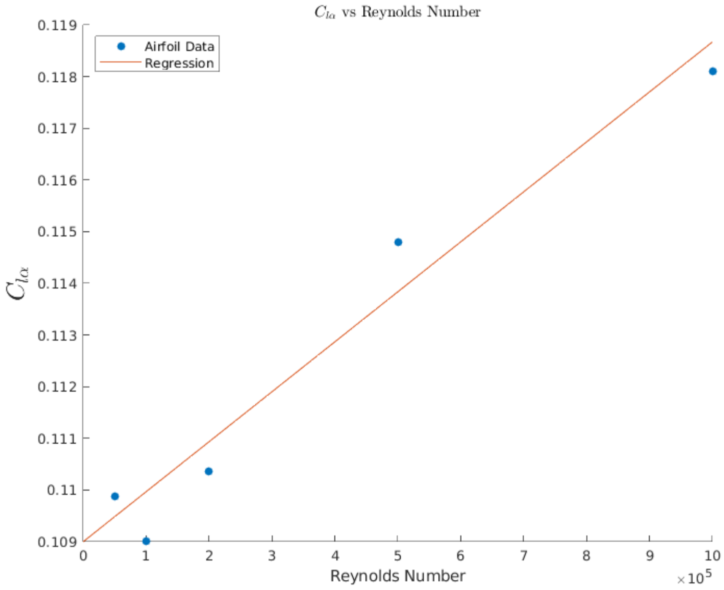

Figure 3.1: Relationship between Reynolds number and $C_{l\alpha}$

3.3 Design Optimization Problem

Two vehicles are considered in this analysis: the 690 AUV developed at Virginia Tech, and the DIVE-LD UUV designed at Virginia Tech and built by Dive Technologies. The hydrodynamic coefficients for the vertical plane of the 690 AUV are presented in Table 3.1. Initial analysis of the DIVE-LD UUV was carried out in the horizontal plane in [21]; the coefficients in the vertical plane for the DIVE-LD UUV are presented in Table 3.2.

For each AUV, we consider two cases: one with the AUV in its nominal configuration, and another where the AUV has a wing between the stern and center of buoyancy (CB). We are interested in static operating conditions that lead to level flight at a constant speed over ground. In particular, we seek operating conditions that use the least energy; therefore, we are interested in finding equilibria that require minimal thrust.

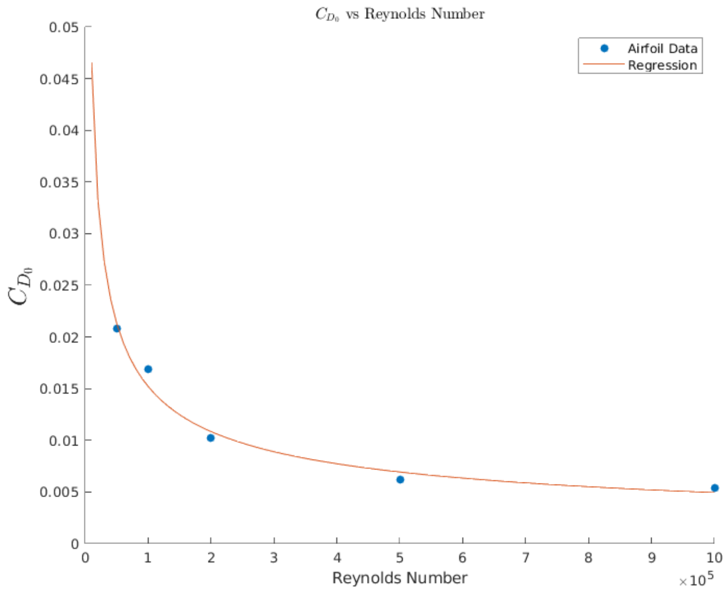

Figure 3.2: Relationship between Reynolds number and C_{D_0}

3.3.1 Wingless AUV

The thrust at a given operating condition and design point, ρ, is expressed as

$$F = F(\nu, \theta, \delta_e, \rho) \tag{3.18}$$

where θ is pitch angle and δ_e is elevator angle. In (3.19), we seek operating points that produce minimal thrust given a set of design variables.

$$\begin{aligned} \delta_e^*, \nu^*, \theta^* = \underset{\nu,\theta,\delta_e}{\operatorname{argmin}} \quad & F(\nu, \theta, \delta_e, \rho)^2 \\ \text{subject to} \quad & \dot{\nu} = 0 \\ & \operatorname{atan}\left(\frac{w}{u}\right) = \theta \\ & v_d = v = \sqrt{\dot{x}^2 + \dot{y}^2} \end{aligned} \tag{3.19}$$

Coefficient	Value
Length (m)	2.194
Width (m)	0.1753
Mass (kg)	47.556
X_{uu} (kg / m)	-4.85
X_{uw} (kg / m)	-0.590297
X_{uq} (kg / rad)	0.0827942
$X_{\dot{u}}$ (kg)	-13.047
X_{ww} (kg / m)	-1.48198
$X_{\dot{w}}$ (kg)	-3.21851
X_{qq} (kg-m / rad^2)	-0.414574
$X_{\dot{q}}$ (kg-m / rad)	0.0329535
$X_{uu\delta\delta}$ (kg / (m-rad^2))	-4.6937
Z_{ww} (kg/m)	-72.497
Z_{qq} (kg-m / rad^2)	-11.824
$Z_{uu\delta}$ (kg / (m-rad))	6.5161
M_{uw} (kg)	26.0741
M_{ww} (kg)	-3.68259
M_{uq} (kg-m/rad)	-22.3806
M_{qq} (kg-m^2/rad^2)	-25.6784
$M_{uu\delta}$ (kg/rad)	6.9036

Table 3.1: 690 AUV hydrodynamic coefficients

where $\dot{\nu}$ is computed by the nonlinear dynamics in (2.8) or (3.1) depending on the vehicle configuration, w is heave velocity and u is surge velocity.

The objective function is squared thrust, which is chosen because thrust corresponds to drag at equilibrium conditions corresponding to constant horizontal motion. We seek to minimize the drag on the hull of a long range AUV, and thus minimize the thrust required for the vehicle operating condition. The constraint $\dot{\nu} = 0$ ensures the vehicle remains at a static operating point corresponding to constant horizontal motion so we can assess that thrust is being used to overcome drag directly. The constraint $\text{atan}\left(\frac{w}{u}\right) = \theta$ ensures the vehicle remains at a constant depth, which is a common performance requirement for long range AUVs. Finally, the constraint $v_d = v = \sqrt{\dot{x}^2 + \dot{y}^2}$ ensures the vehicle maintains a desired

Coefficient	Value
Length (m)	5.42
Width (m)	2
Mass (kg)	4505.58
X_{uu} (kg / m)	-35.2144
$X_{\dot{u}}$ (kg)	-1023.088
$X_{\dot{w}}$ (kg)	0
$X_{\dot{q}}$ (kg-m / rad)	0
$X_{uu\delta\delta}$ (kg / (m-rad^2))	-163.6511
Z_{ww} (kg/m)	-1341.7341
Z_{qq} (kg-m / rad^2)	-1832.7182
$Z_{uu\delta}$ (kg / (m-rad))	262.3615
M_{uw} (kg)	3164.6033
M_{ww} (kg)	-5439.0657
M_{uq} (kg-m/rad)	-4869.2105
M_{qq} (kg-m^2/rad^2)	-4330.2543
$M_{uu\delta}$ (kg/rad)	493.2042

Table 3.2: DIVE-LD UUV hydrodynamic coefficients

speed over ground. This last constraint prevents the vehicle from slowing down in order to get a lower thrust.

We seek to explore how changes in the design space of the vehicle affect the optimal thrust, elevator deflection, and operating conditions. For the nominal configurations of each AUV, the only design variable that can be modified is the buoyancy. Thus, the minimum thrust for each AUV at a set of buoyancies is used to establish a baseline performance for each vehicle.

3.3.2 AUV with a Wing

For an AUV with a wing, the design space is significantly larger than the wingless case. It is of interest to see how changes to the span, chord, wing location and wing angle impacts the operating conditions of the AUV under consideration. The optimization problem in (3.19) is re-purposed to determine the thrust minimal operating conditions for an AUV with a wing.

The wing design variables along with buoyancy are varied systematically for the 690 AUV and the DIVE-LD UUV by considering all possible combinations of a set of design variables. To explore the design space of the 690 AUV, we analyze ten evenly spaced spans between 4cm and 24cm, seven evenly spaced chords between 3cm and 10cm, 21 evenly spaced wing angles from -10 to 10 degrees, and ten wing locations evenly spaced from CB to halfway toward the stern of the vehicle.

Since the DIVE-LD UUV is much larger than the 690 AUV, ten evenly spaced spans between 24cm and 44cm and seven chords between 7cm and 14cm are analyzed for the wing dimensions. All other design variables are in the same ranges as those for the 690 AUV.

3.4 Results

3.4.1 690 AUV

For the 690 AUV, we assess equilibrium drag with and without a wing at 1.5 m/s and 2 m/s. The velocity of 2 m/s velocity is chosen to demonstrate the comparison between the 690 AUV with and without a wing at the 690 AUV's nominal operating speed. The velocity of 1.5 m/s is chosen to demonstrate this same comparison at a slower operating speed that is closer to the energy conservative speeds of long-range AUVs.

The results for the 690 AUV at 2 m/s ground speed are shown in Figure 3.3. The percentage buoyancy range of 0-3% is chosen due to the potential for the vehicle to increase in buoyancy due to variations in water density [28]. The legend denotes the location of the wing, along with its span, s and its chord, c. In this static analysis, thrust is equal to drag. Thus, a lower value for thrust is better for long endurance operations. The optimization procedure finds the smallest wing to be the most efficient, and that no wing configuration is better than the nominal vehicle configuration. We conclude that in this case, the drag induced by the wing is not compensated enough by the lift it generates to improve the amount of body drag the vehicle experiences. Thus, at a 2 m/s ground speed, the 690 AUV does not benefit from a wing.

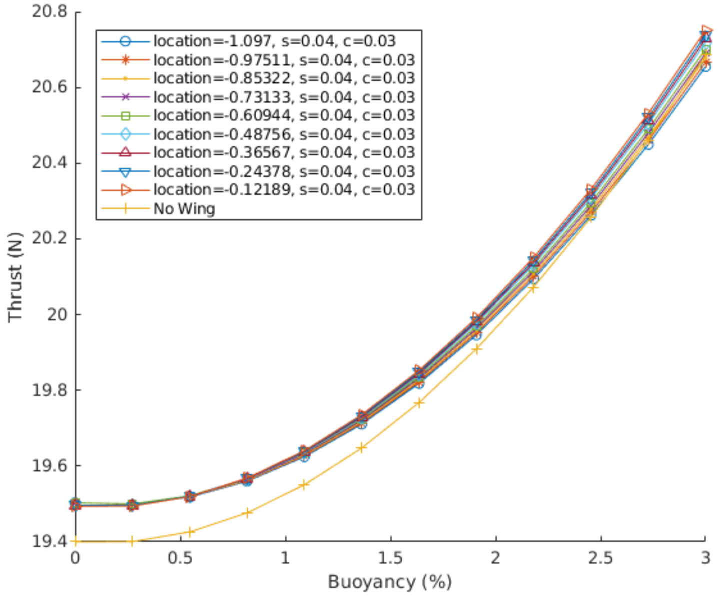

Figure 3.3: Comparison between nominal 690 AUV and optimal static wing configurations at 2 m/s with different buoyancies

The results for the 690 AUV at 1.5 m/s ground speed are shown in Figure 3.4. The optimal wing configuration corresponding to the center of buoyancy location is omitted due to being in stall. These results show that at a slower speed, some wing configurations produce lower drag than the 690 AUV without a wing at higher buoyancies. While the wingless 690 AUV experiences lower drag near 0% buoyancy, the addition of a wing leads to some improvements in net vehicle drag when the vehicle is over 1.5% positively buoyant.

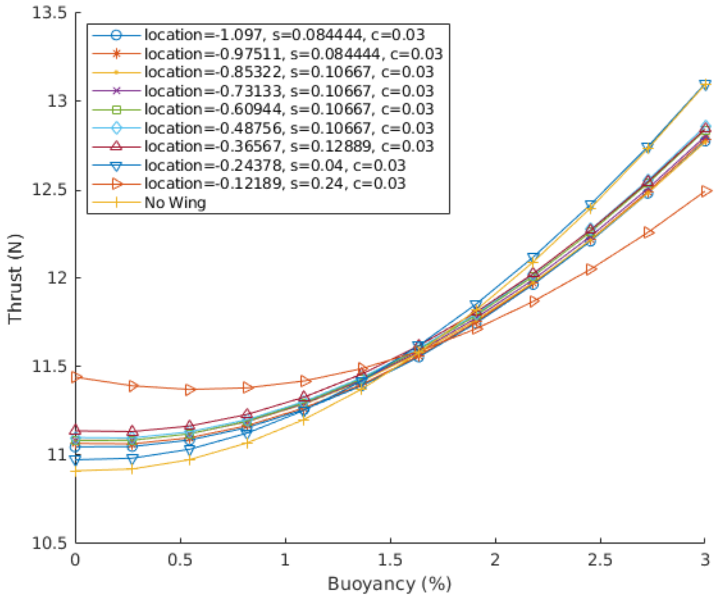

Figure 3.4: Comparison between nominal 690 AUV and optimal static wing configurations at 1.5 m/s with different buoyancies

3.4.2 DIVE-LD UUV

We use the body and control surface geometry of the DIVE-LD UUV, which was designed at Virginia Tech, as another test case. The DIVE-LD UUV geometry is presented in Table 3.2. We assess equilibrium drag with and without a wing at 2 m/s and 3 m/s. The velocity of 2 m/s was chosen to demonstrate a speed on the low end of the DIVE-LD speed range, which could be used for long range missions. The velocity of 3 m/s is chosen to demonstrate how adding a wing to the DIVE-LD UUV affects the thrust required at a typical operating speed.

The resulting thrust requirements for the DIVE-LD UUV at 3 m/s are shown in Figure 3.5. The thrust is equivalent to drag, so lower thrust indicates the vehicle will experience lower drag, which is ideal for long endurance missions. For low buoyancy percentages at this speed, the addition of a wing either keeps similar performance, or degrades performance. As the percentage buoyancy increases however, the addition of a wing becomes more effective as the wing is more efficient at generating downforce than the hull or rear control surfaces. Thus, we can see that the addition of a wing for the DIVE-LD UUV at nominal operating conditions may be appropriate.

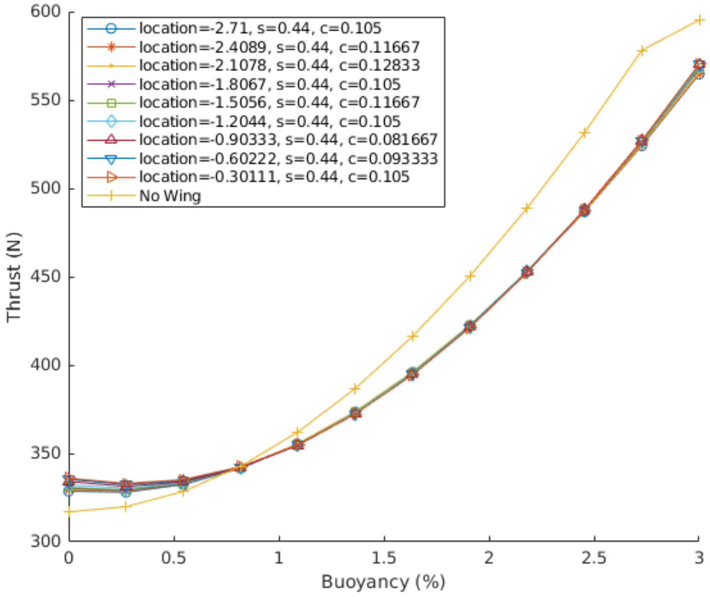

Figure 3.5: Comparison between nominal DIVE-LD UUV and optimal static wing configurations at 3 m/s with different buoyancies

Thrust for the case of 2 m/s is shown in Figure 3.6. A buoyancy range of 0 to 1% is chosen due to the vehicle being less stable at this speed. In this case, we see that a high aspect ratio wing is able to achieve better performance than the wingless vehicle for $|b| > 0.4\%$, where b is the percent buoyancy.

3.5 Conclusions

In this chapter, a design exploration procedure is demonstrated for the selection of wing design parameter values. The dynamic model for a wing is shown and regression analysis is

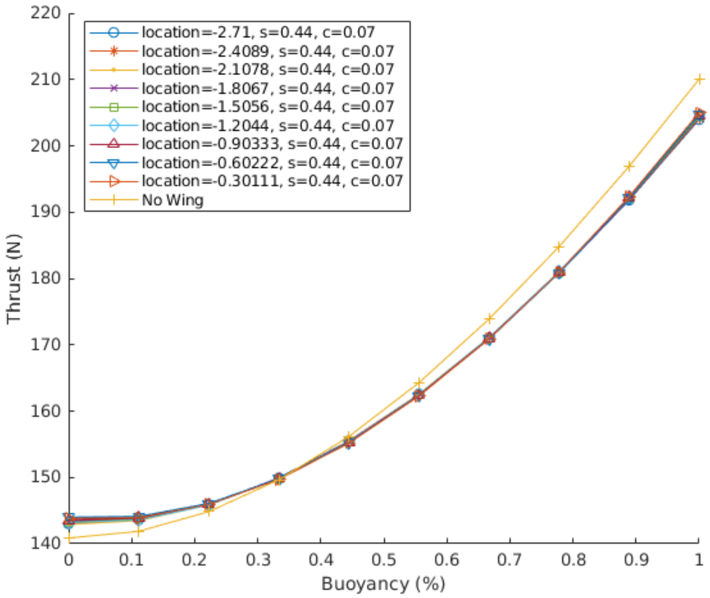

Figure 3.6: Comparison between nominal DIVE-LD UUV and optimal static wing configurations at 2 m/s with different buoyancies

used to relate variable Reynolds numbers to lift and drag coefficient values. An optimization problem is solved to find thrust minimal operating points for an AUV with and without a wing to demonstrate how wing design impacts vehicle endurance with respect to thruster output. A design exploration procedure is used to understand the design tradeoffs in adding a wing. The wing is shown to be effective at slow speeds for two AUVs if either vehicle is significantly positively buoyant. Furthermore, the addition of a wing for the DIVE-LD UUV would improve its thruster energy use at a higher speed.

Chapter 4

Controller Design and Evaluation

4.1 Introduction

For long endurance AUVs, energy used by the control system impacts vehicle range. In this chapter, we propose a method for relating AUV design parameters to the energy used by the vehicle's actuators during a mission. By investigating how loop-shaping characteristics influence the energy used by the control system of a long range AUV, we seek to understand how energy considerations impact other areas of control performance.

Maximizing vehicle endurance is critical for deployed robotics applications. Prior work in mobile robotics focused on planning a minimal energy path based on data collected at different motor speeds [18]. For unmanned aerial vehicles (UAVs), motion planning research has focused on considering the effort used by a quadcopter's motors in planning minimum energy paths [20]. For the AUV control problem, a nonlinear control method was developed that considers the approximate energy used by the actuators while using an optimal control technique [5]. Recent work developed an Economic Model Predictive Control (EMPC) system to minimize the energy used by thrusters that control the attitude of an AUV [34]. The goal of this chapter is to describe a preliminary analysis on assessing and reducing the energy required by an AUV control system. In other words, we seek to understand if endurance can be increased simply by implementing a control system that requires less energy.

It is intuitively reasonable that a control system for a long-endurance AUV should minimize the motion of control surfaces, and thus minimize the energy needed for control [28]. Furthermore, the general relationship between system bandwidth and typical control performance objectives is well-understood. Less-well understood is the specific relationship between the energy used by the control surface actuators of an AUV and typical control performance objectives. By explicitly evaluating energy needed for control, we show that a significant reduction in energy needed for control can be achieved with only small reductions in control system performance.

In [12], the authors use loop-shaping techniques to design attitude controllers for the 690s AUV at Virginia Tech. In this work, the authors use the loop-shaping technique found in [19] to develop robust $\mathcal{H}_\infty$ controllers to show the tradeoff between fin angle commands and tracking performance. However, this does not specifically consider actuator energy used, or vehicle agility.

In this chapter we evaluate performance metrics that are useful for assessing AUV control performance. We investigate how various loop-shaping characteristics may influence control system performance with respect to our proposed metrics. We then leverage our findings to account for tradeoffs between tracking performance, energy use and vehicle agility during the design of an $\mathcal{H}_\infty$ pitch-axis controller for the 690 AUV.

4.2 Performance Metrics

A common practice is to implement depth control with an inner-loop pitch controller that accept pitch reference commands from an outer-loop depth controller. The pitch control inner-loop is usually faster than the depth control outer-loop; the time-scale separation ensures that the actual depth control performance of the closed-loop system is similar to the expected performance. Therefore, for this preliminary analysis, we focus on the faster pitch-control loop, since we expect it to have a greater impact on the energy used by control surface servos.

For our control system design problem, the performance metrics we seek to evaluate the energy cost of actuator effort, reference tracking error, and vehicle agility, which is characterized by step-response performance.

4.2.1 AUV Dynamics

The analysis in this chapter is performed on a numerical simulation of the 690 AUV developed at Virginia Tech. The 690 AUV is a typical streamlined tail-controlled AUV for which a high fidelity nonlinear model exists. The hydrodynamic coefficients for the 690 AUV are presented in Table 3.1. From [22], the dynamics are summarized

$$\dot{\nu} = f(\nu, u) = M^{-1} \left(C_a \nu - C_{rb} \nu + D\nu + G + \tau \right) \tag{4.1}$$

This model is used to assess performance of our control system. For a desired buoyancy of the vehicle we use the nonlinear model to find an operating point corresponding to level flight at 2 m/s.

4.2.2 Control Energy Cost

For long endurance vehicles, minimizing energy used by the controller is important as missions can last for days at a time [28]. For the 690 AUV, there are two primary ways energy is used by the control system: via the thruster that propels the vehicle forward, and the servo motors used to control the fins. For the thruster, we take the vehicle drag in a static setting to be analogous with the energy used. To model actuator energy use, we develop the linear servo model shown in Figure 4.1 to understand the dynamic case.

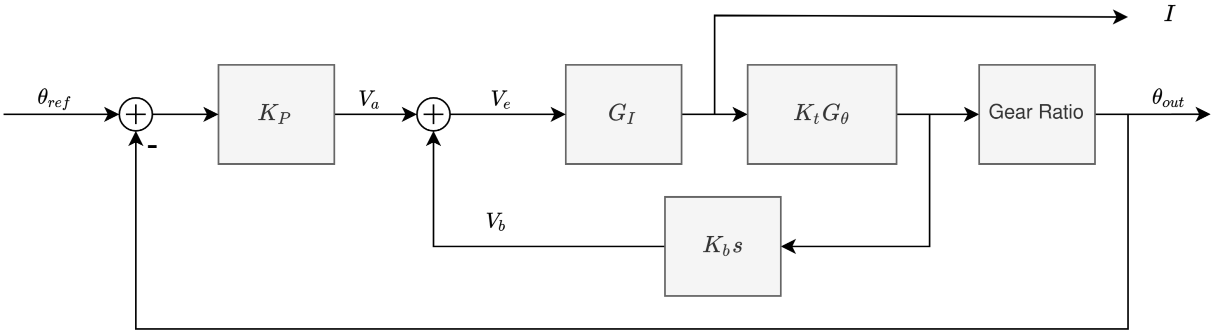

Figure 4.1: Servo block diagram

The internal servo controller attempts to drive the output angle θ_{out} to the reference angle θ_{ref}. We model the internal servo controller as a proportional controller with gain K_P

$$u = K_P \theta_{error} = K_P(\theta_{ref} - \theta_{out}) \tag{4.2}$$

The internal servo controller commands an armature voltage V_a. The servo circuitry is designed to drive the motor back-EMF V_b to be equal to V_a. We relate the motor shaft angle before gearing to the back-EMF of the motor via the constant K_b

$$V_b = K_b \frac{d\theta_i}{dt} \tag{4.3}$$

Referencing Figure 4.2 and using Kirchhoff's voltage law, we can see that $V_e = V_a - V_b$ is the voltage drop across the resistor, R and inductor, L. Thus we have the transfer function from voltage difference to armature current

$$G_I(s) = \frac{1}{R + sL} \tag{4.4}$$

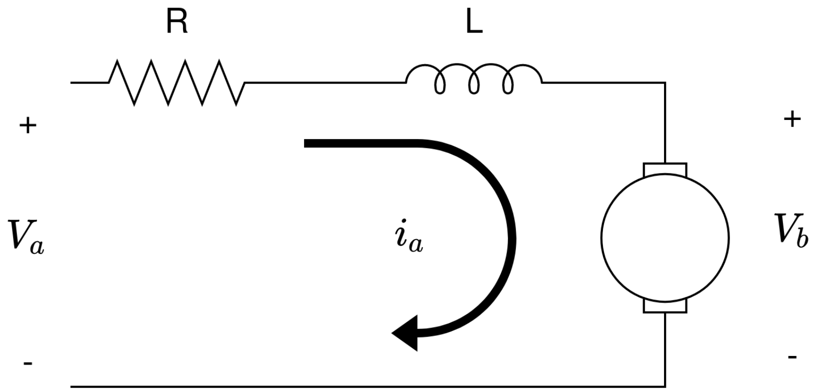

Figure 4.2: Armature servo circuit

Motor angle is related to torque applied to the motor shaft, which is related to the armature current i_a. We have a torque constant K_t that relates armature current to torque applied to the motor shaft

$$\tau(t) = K_t i_a(t) \tag{4.5}$$

Finally, we take G_θ to be the transfer function from torque to internal shaft angle

$$G_\theta(s) = \frac{1}{Js^2 + Ds} \tag{4.6}$$

For the 690 AUV, the Futaba BLS173SV servo is used to control the vehicle's fin angles. The specification of the servo motor are shown in Table 4.1.

In order to approximate this servo's performance in simulation, we perform an optimization procedure to select servo model coefficients to achieve similar speed characteristics for the 6V case. J and D were determined to be much smaller numbers than the other coefficients,

Characteristic	Value
Speed at 6V	0.12 sec / 690°
Speed at 6.6V	0.11 sec / 60°
Speed at 7.4V	0.10 sec / 60°
Weight	28g
Dimensions	33mm x 15 mm x 27 mm

Table 4.1: Futaba BLS137SV servo motor characteristics [2]

and were set to constant values. For the remaining coefficients we have

$$\begin{aligned} K_t^*, K_b^*, R^*, L^*, K_P^* = \underset{K_t, K_b, R, L, K_P}{\operatorname{argmin}} \quad & (\theta_{out_{0.12}} - 60^\circ)^2 + \|M_{\theta_{out}}\|_\infty \\ \text{subject to} \quad & 0 \leq K_t \leq 0.1 \\ & 0 \leq K_b \leq 0.01 \\ & 0.5 \leq R \leq 10 \\ & 0 \leq L \leq 0.001 \\ & K_P \geq 0 \\ & i_{max} < 1 \\ & V_{max} < 6.6 \end{aligned} \tag{4.7}$$

where $\theta_{out_{0.12}}$ is the resulting trajectory at the 6V time to reach 60 degrees, and $M_{\theta_{out}}$ is the linear operator for the servo output angle. By minimizing the $\mathcal{H}_\infty$ norm of this system, the optimizer attempts to enforce stability of the servo model in θ_{out}. The other constraints are chosen to ensure the servo remains in a reasonable operating space. By running this optimization procedure, we get a servo model that achieves the desired speed with the coefficients in Table 4.2 and is stable. The servo motor trajectory for the configuration found when commanded to sweep 20 degrees is shown in Figure 4.3.

Coefficient	Value
K_t	0.082118 Nm / A
K_b	6.68×10^{-4} V/(rad/s)
R	5.396193 ohms
L	507 μH
K_P	4.085
J	5×10^{-7} kg-m^2
D	8×10^{-6} Nm / (rad/s)

Table 4.2: Servo Coefficient Estimates

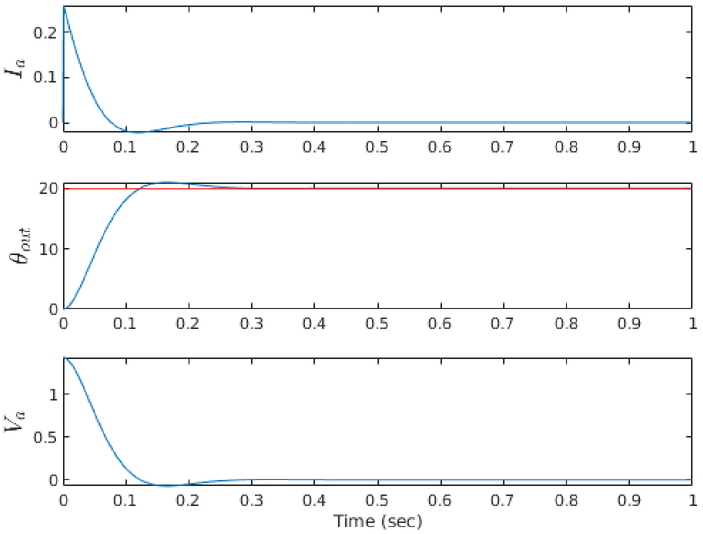

Figure 4.3: Current, angle, and armature voltage trajectory for the servo motor

Let $I = i_a$ be the current used by the servo motor. From the servo model we capture power usage through the outputs V_a and I, which gives us the actuator power, P

$$P = IV_a \tag{4.8}$$

This allows us to compute the energy in joules used over the course of a trajectory

$$E = \int_0^{t_f} P(t)dt \tag{4.9}$$

which over the course of our experiments is approximated using a trapezoidal numerical integration technique

$$E \approx \frac{1}{2}\sum_{k=0}^{N}(t_{k+1} - t_k)\left[P_{k+1} + P_k\right] \tag{4.10}$$

4.2.3 Tracking Error

In our analysis, tracking error is used to quantify how well a controller performs given an operating condition and an actuator disturbance. Specifically, we take the tracking error, e_t to be the averaged root mean square (RMS) of an error trajectory e at steady state

$$e_t = \frac{1}{t_f - t_0}\left(\int_{t_0}^{t_f} |e(t)|^2 dt\right)^{\frac{1}{2}} \tag{4.11}$$

where $e(t)$ is the error trajectory of interest. For our control design problem, we use pitch tracking error, θ_e to evaluate and compare our controllers.

4.2.4 Agility

In Chapter 2, maneuvering performance was assessed using open-loop step responses. To evaluate the agility of the control system for our AUV, we can take a similar approach in the closed-loop case.

For an underwater vehicle, we define agility as the reactiveness of the control system to a change in the reference trajectory. To measure the reactiveness of the AUV, we compute the rise time of the pitch of the vehicle when given a step response in the pitch command.

4.3 Modeling Characteristics

In this section we describe the modeling characteristics that impact AUV control system design. We specifically focus on developing an actuator disturbance, and on the influence of sensitivity functions on linear systems.

4.3.1 Actuator Disturbance

Steady maneuvering performance is observed for simulated models of AUVs, but unsteady behavior is observed in actual AUVs. We seek to inject a disturbance that generates non-steady behavior in the simulated model. For this control problem, we choose to apply an actuator disturbance. This choice is due to an actuator disturbance being physically plausible, and because it generates non-steady motion matching the behavior of the 690 AUV in the field.

For a commanded fin angle f_c, let the true fin angle f be affected by some disturbance d_f

$$f(t) = f_c(t) + d_f(t) \tag{4.12}$$

Let the actuator disturbance be represented by brown noise, $D_b(t)$, with a bandwidth of 10 Hz. To vary the disturbance amplitude, a disturbance gain, K_d, is applied. Thus the disturbance is modeled as

$$d_f(t) = K_d D_b(t) \tag{4.13}$$

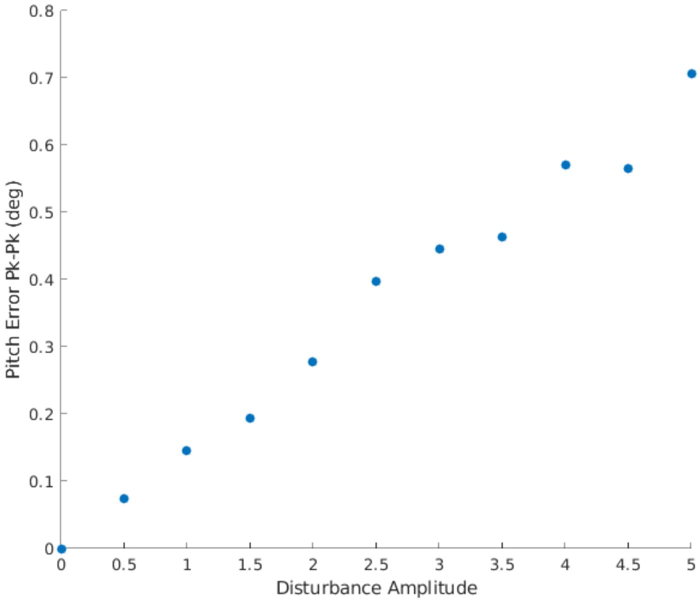

Figure 4.4: Effect of different values for K_d on peak to peak error in simulated pitch

We apply varying levels of disturbance amplitude to a linearized dynamical model in simulation and get different peak to peak errors in pitch, as shown in Figure 4.4. The pitch error trajectories for three example disturbances are shown in Figure 4.5. When analyzing field data from the vehicle on a straight path near a constant depth, we get similar peak to peak oscillations in pitch error to what we see in a simulated disturbance when $1 < K_d < 2$, as seen in Figure 4.6.

4.3.2 Loop Shaping Functions

From [9], let Figure 4.7 be a general multi input-multi output (MIMO) system with plant $P(s)$ and controller $C(s)$. The sensitivity function takes the input and output forms S_i and S_o respectively

$$\begin{aligned} S_i &= (I - CP)^{-1} \\ S_o &= (I - PC)^{-1} \end{aligned} \tag{4.14}$$

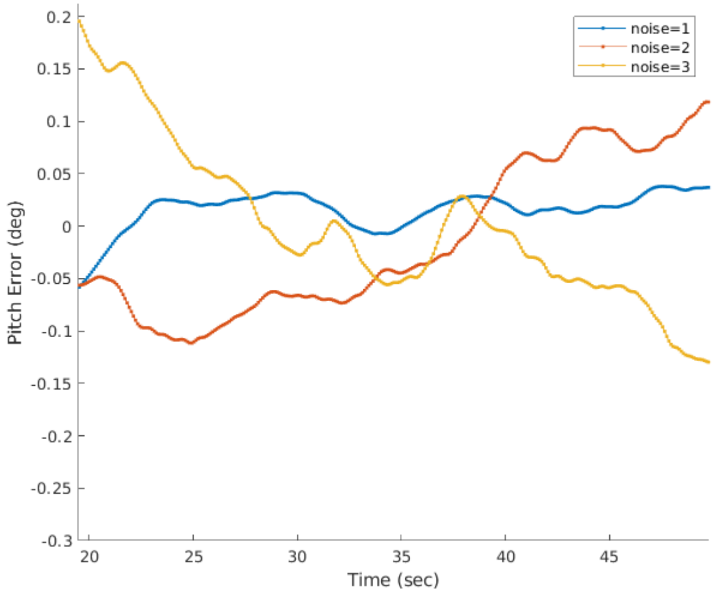

Figure 4.5: Simulated pitch error at $K_d = 1, 2, 3$

and the complementary sensitivity function takes a similar form

$$\begin{aligned} T_i &= CP(I - CP)^{-1} \\ T_o &= PC(I - PC)^{-1} \end{aligned} \tag{4.15}$$

Thus for a MIMO system, we have the system responses (4.16), (4.17), and (4.18).

$$Y = S_o D_o, + S_o P D_i + T_o(R - N) \tag{4.16}$$

$$E = S_o(R - D_o - N - PD_i) \tag{4.17}$$

$$U = CS_o(R - N - D_o) - T_i D_i \tag{4.18}$$

Let $\bar{\sigma}(\cdot)$ be the maximum singular value for a transfer function. We can see from (4.16) that large $\bar{\sigma}(S_o)$ in the frequency band of the actuator disturbance will result in the disturbance having a large effect on the output if $\bar{\sigma}(P)$ is also large at the same frequency band. For

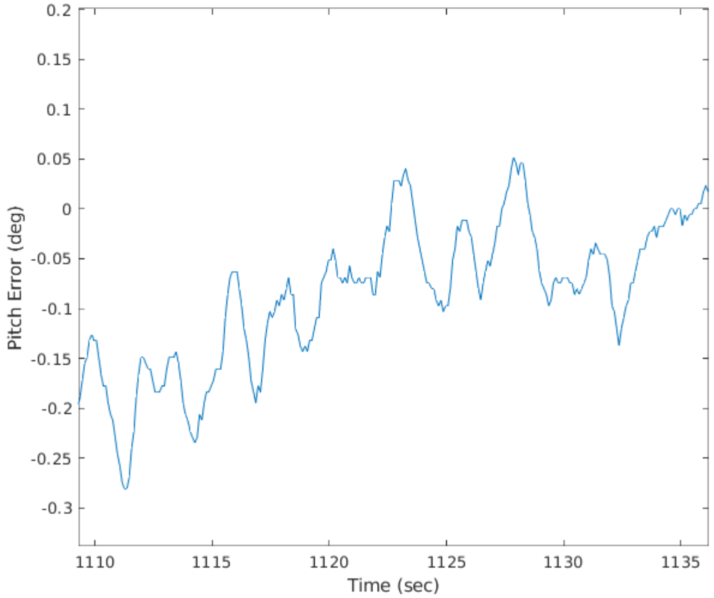

Figure 4.6: Field data with a PID autopilot shows about ±0.2 degrees of peak to peak oscillations in pitch error

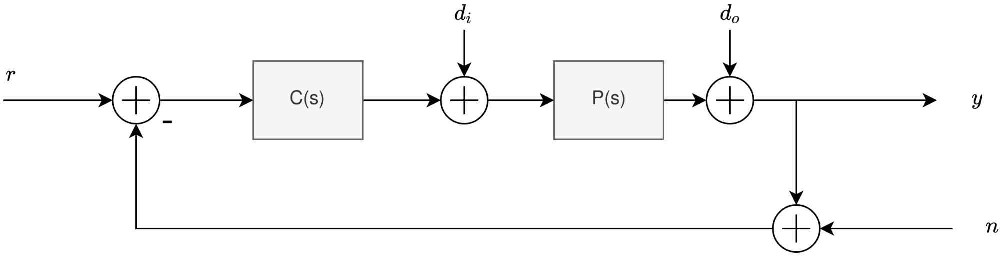

Figure 4.7: Multi Input Multi Output Feedback System

systems with an actuator disturbance, input complementary sensitivity T_i also plays a role as shown in (4.18). If $\bar{\sigma}(T_i)$ is large in the frequency band of the disturbance, then the disturbance will affect the control signal.

4.4 Sensitivity Relationship to Performance

In order to gain initial insights in how the 690 AUV is impacted by loop-shaping design choices, we systematically vary the loop gain and evaluate energy use and control system performance. Specifically, we run the system with a stabilizing proportional controller and iteratively change the gains. We perform these tests at a range of buoyancies on the 690 AUV dynamics linearized around operating points corresponding to level flight.

The tradeoff in the energy cost of maintaining steady state and the tracking error of the vehicle is investigated through simulation. The vehicle is commanded to maintain a steady state operating condition for 60 seconds to measure the energy cost of maintaining the operating point and the tracking performance. Then, for 40 seconds a five degree pitch step command is applied to assess agility.

The proportional gains tested for this analysis are $G = \{2, 3, 4, 5, 6, 7, 8, 9, 10\}$. When simulating the AUV, we apply an actuator disturbance (4.13). Ten disturbance trajectories are generated *a priori* corresponding to ten runs, in order to ensure the results from each gain are compared to each other with the exact same underlying disturbances. Results are averaged over these ten runs in order to extract trends from the data. While we test many buoyancies and disturbances, we report results from the simulation that seem to most closely match the 690 AUV. We simulate the buoyancy of the 690 AUV at 0.2%, and the actuator disturbance variance is chosen to have amplitude $K_d = 1.5$ in accordance with Section 4.3.1.

The simulated vehicle is commanded to remain at steady state operating conditions for the first 60 seconds, and is then commanded to perform a step change in pitch angle. The tradeoff between energy cost, agility and tracking error with respect to peak sensitivity across all frequencies, $\bar{\sigma}(S_o)$ is shown in Figure 4.8. Similarly, for peak complementary sensitivity, $\bar{\sigma}(T_i)$ the tradeoff is shown in Figure 4.9. These tradeoffs indicate that low peak gains for S_o

and T_i yield lower energy usage than higher peak gains. Additionally, we can see that low energy usage can be achieved without much sacrifice in agility or tracking error.

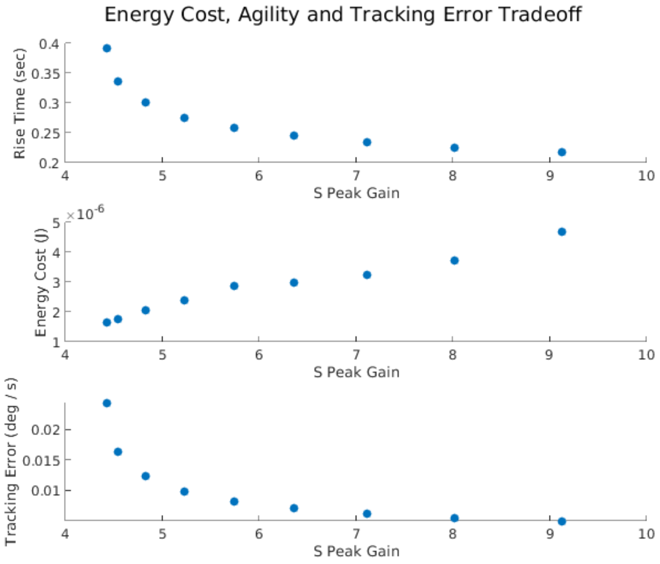

Figure 4.8: Performance vs peak sensitivity. Energy use can be reduced with only a small performance reduction

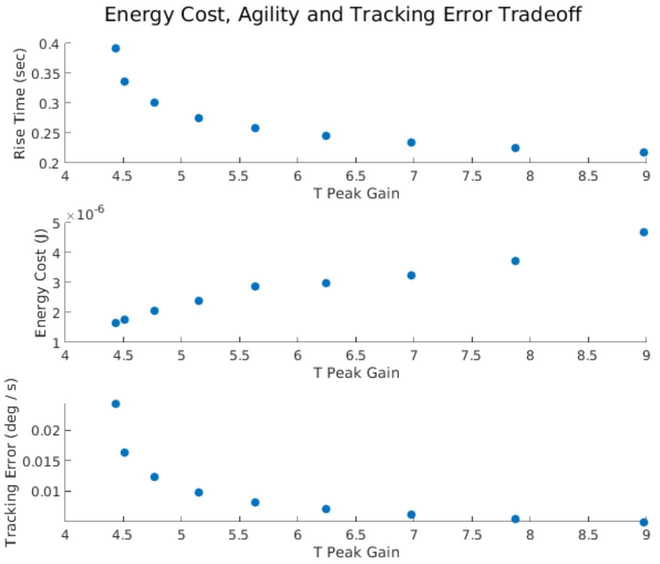

Figure 4.9: Performance tradeoffs for peak complementary sensitivity

4.5 $\mathcal{H}_\infty$ Control Design

Given the proposed disturbance model for the 690 AUV and the relationship between design specifications and control performance, we seek to design a controller that is robust to the actuator disturbance modeled for the 690 AUV.

The $\mathcal{H}_\infty$ norm of an operator G is defined as

$$\|G\|_\infty = \sup_\omega \bar{\sigma}(G(j\omega)) \tag{4.19}$$

where $\bar{\sigma}(\cdot)$ is the maximum singular value. If $y = Gu$, then

$$\|y\|_{L_2} \leq \|G\|_\infty \|u\|_{L_2} \tag{4.20}$$

So $\|G\|_\infty$ can be interpreted as the worst-case L_2 gain. Since L_2 gain is related to the energy gain of the system [8], we seek to design weighting functions such that the closed loop system is stable and the $\mathcal{H}_\infty$ norm of the system is minimized.

For our control synthesis problem, we have the unweighted system diagram scheme shown in Figure 4.10.

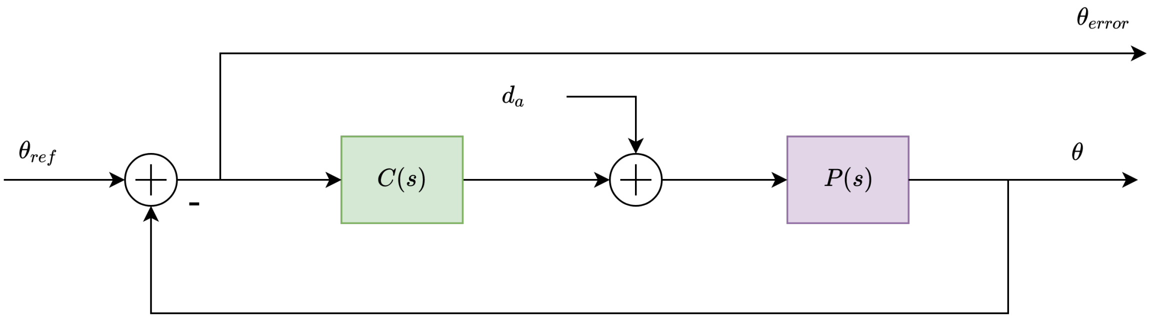

Figure 4.10: AUV pitch axis system diagram

Let the unweighted outputs $\bar{z}$ and unweighted inputs $\bar{w}$ be defined as

$$\bar{z} = \begin{bmatrix} \theta_{error} & \theta \end{bmatrix}^\intercal \quad \text{and} \quad \bar{w} = \begin{bmatrix} \theta_{ref} & d_a \end{bmatrix}^\intercal \tag{4.21}$$

We define $P(s)$ as being partitioned

$$P(s) = \begin{bmatrix} P_{11}(s) & P_{12}(s) \\ P_{21}(s) & P_{22}(s) \end{bmatrix} \tag{4.22}$$

such that we have the relationship between system inputs and outputs

$$\begin{bmatrix} \bar{z} \\ e \end{bmatrix} = P(s) \begin{bmatrix} \bar{w} \\ u \end{bmatrix} = \begin{bmatrix} P_{11}(s) & P_{12}(s) \\ P_{21}(s) & P_{22}(s) \end{bmatrix} \begin{bmatrix} \bar{w} \\ u \end{bmatrix} \tag{4.23}$$

which yields the system diagram shown in Figure 4.11.

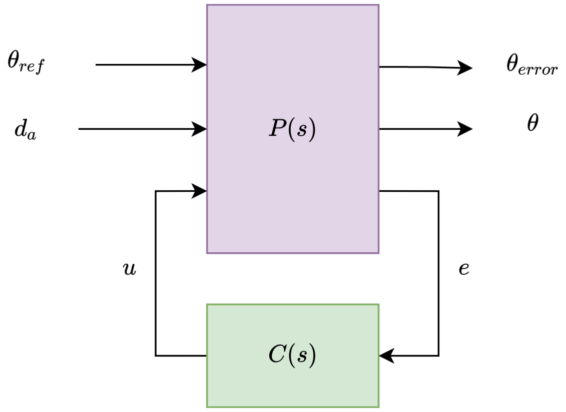

Figure 4.11: Unweighted $\mathcal{H}_\infty$ model for the AUV pitch control problem.

From [8], we have that the linear fractional transformation is the transfer function from $\bar{w}$ to $\bar{z}$ in Figure 4.11, defined as

$$\underline{S}(P, C) = P_{11} + P_{12}C(I - P_{22}C)^{-1}P_{21} \tag{4.24}$$

We add weighting functions to the system to design a controller with specific performance characteristics. We seek to reject actuator disturbance and shape the sensitivity and complementary sensitivity functions. To this end, we have the weighting scheme shown in Figure 4.12.

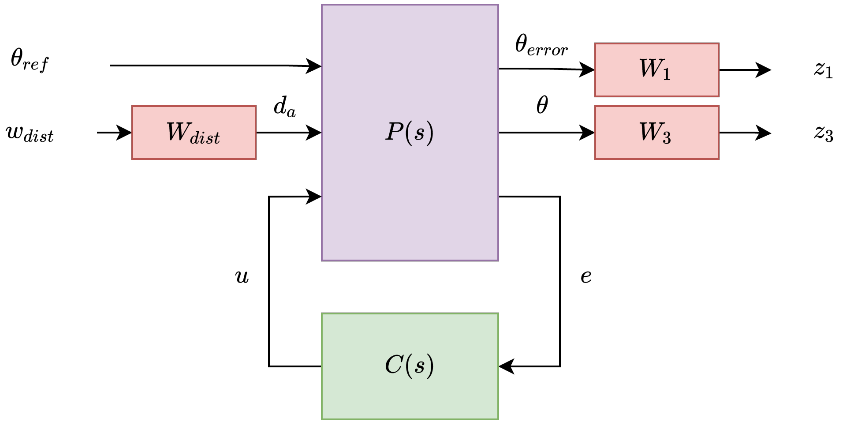

Figure 4.12: Weighted $\mathcal{H}_\infty$ model for the AUV pitch control problem.

Let the weighted performance outputs, z, and exogenous inputs, w, be defined as

$$z = \begin{bmatrix} z_1 & z_3 \end{bmatrix}^\intercal \quad \text{and} \quad w = \begin{bmatrix} \theta_{ref} & w_{dist} \end{bmatrix}^\intercal \tag{4.25}$$

For the inputs, we define the weight matrix W_w

$$W_w(s) = \begin{bmatrix} 1 & 0 \\ 0 & W_{dist}(s) \end{bmatrix} \tag{4.26}$$

and for the outputs we have the weight matrix W_z

$$W_z(s) = \begin{bmatrix} W_1(s) & 0 \\ 0 & W_3(s) \end{bmatrix} \tag{4.27}$$

As shown in [24], we can append the weighting matrices to $P(s)$ in the form shown in Figure 4.12. Let the resulting transfer function from w to z be M

$$M(s) = W_z(s)\underline{\mathrm{S}}(P, C)W_w(s) \tag{4.28}$$

where $\underline{\mathrm{S}}(P, C)$ is the linear fractional transformation of the unweighted system found in (4.24). We can expand to explicitly solve for $M(s)$

$$M(s) = W_z(s)\left[P_{11} + P_{12}C(I - P_{22}C)^{-1}P_{21}\right]W_w(s) \tag{4.29}$$

Thus we have that $M(s)$ takes the form of the lower linear fractional transformation of the weighted system, and relates w to z

$$z = M(s)w = W_z(s)\left[P_{11} + P_{12}C(I - P_{22}C)^{-1}P_{21}\right]W_w(s)w \tag{4.30}$$

We seek a controller $C(s)$ that minimizes $\|M(s)\|_\infty$ such that $\|M(s)\|_\infty < 1$. Modifying (4.17) and (4.16) to add the weighting filters while only considering reference and actuator disturbance inputs we have

$$z_1 = W_1E = W_1(S_oR - S_oPW_{dist}D_i) \tag{4.31}$$

$$z_3 = W_3Y = W_3(S_oPW_{dist}D_i + T_iR) \tag{4.32}$$

which when put into matrix form gives

$$\begin{bmatrix} z_1 \\ z_3 \end{bmatrix} = \underbrace{\begin{bmatrix} W_1S_o & -W_1S_oPW_{dist} \\ W_3T_i & W_3S_oPW_{dist} \end{bmatrix}}_{M(s)} \underbrace{\begin{bmatrix} R \\ D_i \end{bmatrix}}_{w} \tag{4.33}$$

Thus we see that by minimizing $\|M(s)\|_\infty$, the weighting filters W_1 and W_3 shape the output sensitivity function S_o and the input complementary transfer function T_i.

The weighting function to reject disturbances, W_{dist} is chosen to be a low-pass filter of the form

$$W_{dist}(s) = \frac{0.1s + 2}{s + 2} \tag{4.34}$$

to reject low frequency disturbances such as incorrect fin positions or slow actuator disturbances as shown in Section 4.3.1.

The weighting function W_3 has the most impact on T_i. We have that

$$\|T_i\|_\infty \lessapprox \gamma\bar{\sigma}(W_3^{-1}) \tag{4.35}$$

In order to achieve low actuator energy use, W_3 is chosen to keep the peak gain for T_i low as informed by Figure 4.9. Thus, the exact filter chosen is a high-pass filter of the form

$$W_3(s) = \frac{1.43s + 178.5}{s + 198} \tag{4.36}$$

The weighting function W_1 is used to design S_o. We have that

$$\|S_o\|_\infty \lessapprox \gamma\bar{\sigma}(W_1^{-1}) \tag{4.37}$$

Thus, the peak gain of W_1^{-1} is related to the energy used by the controller. A low-pass filter is chosen for W_1 in order to penalize tracking error at low frequencies. A small bandwidth is chosen to focus the penalty on the lowest frequencies. We parameterize the design for W_1 as follows

$$W_1(s) = \frac{\frac{1}{W_g}s + W_g \times 10^{-3}}{s + 1 \times 10^{-3}} \tag{4.38}$$

where W_g is the desired maximum peak gain for S_o, which is used to determine the energy used by the control system. From Figure 4.8, we take $W_g = 5$ due to this peak sensitivity having low energy cost, with moderate tracking error and rise time compared to other peak sensitivities. This results in

$$W_1(s) = \frac{\frac{1}{5}s + 5 \times 10^{-3}}{s + 1 \times 10^{-3}} \tag{4.39}$$

From this design analysis, we expect that in our experiments our controller will have a low energy cost, without sacrificing much tracking performance or agility.

4.6 Experimental Results

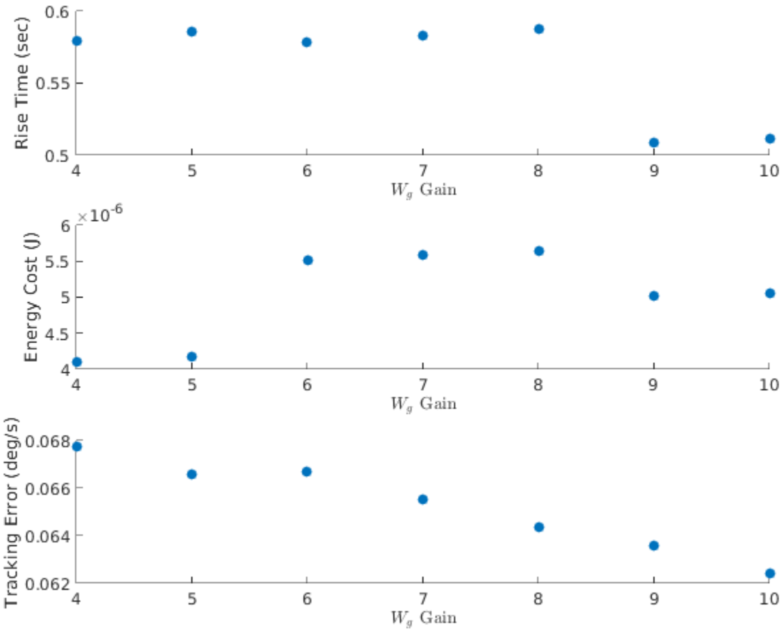

Figure 4.13: Performance tradeoffs for various choices of gain W_g for W_1 at $K_d = 1.5$ disturbance gain

We perform experiments by simulating the 690 AUV nonlinear dynamics with our $\mathcal{H}_\infty$ controller. We analyze the performance of our controller by commanding it to maintain steady state for 60 seconds and then commanding a five degree pitch step, as in Section 4.4.

The comparison between different choices for W_g is shown in Figure 4.13. The relationships in this figure are noisy due to simulating with the nonlinear dynamics. As expected, the controller at $W_g = 5$ is energy efficient with some minimal tradeoffs in tracking performance. Our controller is the second most energy efficient in the comparison. As a tradeoff, our controller has higher tracking error and a higher rise time (indicating lower agility) than the other controllers. However, the tracking error drawbacks are small as expected from our sensitivity investigation. An example trajectory of pitch error for our chosen controller is shown in Figure 4.14. As can be seen in this figure, the controller has acceptable performance at tracking steady state references.

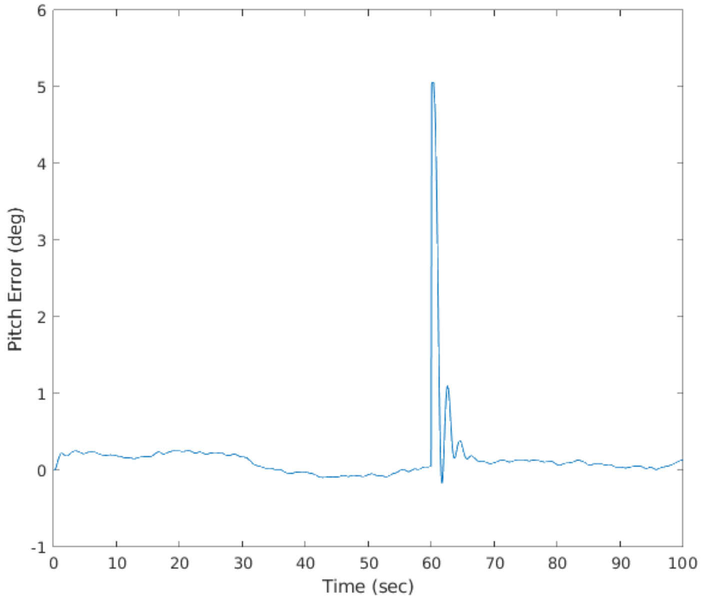

Figure 4.14: Nonlinear simulation trajectory for pitch error with $W_g = 5$ at $K_d = 1.5$ actuator disturbance gain

Chapter 5

Conclusions

The relationships shown between loop-shaping function parameters were shown to be useful in designing an $\mathcal{H}_\infty$ controller to meet performance objectives for the 690 AUV. An energy efficient controller is developed to show that actuator energy consumption can be reduced with only a small reduction in other performance objectives for AUVs. Future work will fully explore the design space of the control system beyond using a proportional controller to modify the loop-shaping functions. A rigorous theoretical analysis that relates loop-shaping design choices to AUV performance may be even more insightful than the technique presented. It is also of interest to verify the proposed control design method using field trials.

The addition of a wing is considered to reduce the thrust used by the 690 AUV and the DIVE-LD UUV. Future work can build on this analysis by considering the airfoil type and wing shape in the design space exploration. Additional work that relates AUV design to the benefits of a wing can lead to better performance for long endurance AUVs. Developing an understanding of how vehicle design impacts wing requirements may allow future work to better determine when a wing is needed for a long endurance AUV.

Additionally, work that builds on the analysis in Chapter 2 by relating AUV design parameters to hydrodynamic coefficients and hence to vehicle maneuvering performance can improve the understanding of how AUV plant design affects control performance. By rigorously tracking uncertainty throughout the design process, additional work can be done to find controllers that are more robust to specific design uncertainties of an AUV.

Bibliography

[1] NACA 0012 airfoils (n0012-il). URL http://airfoiltools.com/airfoil/details?airfoil=n0012-il.

[2] Futaba BLS173SV - HV S.BUS2 programmable mini air servo. URL https://servodatabase.com/servo/futaba/bls173sv.

[3] Induced drag coefficient, May 2021. URL https://www.grc.nasa.gov/www/k-12/airplane/induced.html.

[4] Abbott Ira H A. and Von Doenhoff Albert E. *Theory of wing sections: Including a summary of airfoil data*. Dover, 1959.

[5] Mehmet Selcuk Arslan, Naoto Fukushima, and Ichiro Hagiwara. Nonlinear optimal control of an AUV and its actuator failure compensation. In *2008 10th International Conference on Control, Automation, Robotics and Vision*, pages 668–673, 2008. doi: 10.1109/ICARCV.2008.4795597.

[6] James G. Bellingham, Yanwu Zhang, Justin E. Kerwin, Jonathan Erikson, Brett Hobson, Brian Kieft, Michael Godin, Robert McEwen, Thomas Hoover, James Paul, Andrew Hamilton, Jeffrey Franklin, and Andrew Banka. Efficient propulsion for the Tethys long-range autonomous underwater vehicle. In *2010 IEEE/OES Autonomous Underwater Vehicles*, pages 1–7, 2010. doi: 10.1109/AUV.2010.5779645.

[7] Ryan G. Coe and Wayne L. Neu. Amplitude effects on virtual PMM tests. In *2012 Oceans*, pages 1–5, 2012. doi: 10.1109/OCEANS.2012.6405027.

[8] Geir E. Dullerud and Fernando Paganini. *A course in robust control theory: A convex approach*. Springer, 2005.

[9] J. Freudenberg, R. Middleton, and A. Stefanpoulou. A survey of inherent design limitations. In *Proceedings of the 2000 American Control Conference. ACC (IEEE Cat. No.00CH36334)*, volume 5, pages 2987–3001 vol.5, 2000. doi: 10.1109/ACC.2000.879113.

[10] Maaten E. Furlong, Stephen D. McPhail, and Peter Stevenson. A concept design for an ultra-long-range survey class AUV. In *OCEANS 2007 - Europe*, pages 1–6, 2007. doi: 10.1109/OCEANSE.2007.4302453.

[11] Maaten E. Furlong, Dave Paxton, Peter Stevenson, Miles Pebody, Stephen D. McPhail, and James Perrett. Autosub Long Range: A long range deep diving AUV for ocean monitoring. In *2012 IEEE/OES Autonomous Underwater Vehicles (AUV)*, pages 1–7, 2012. doi: 10.1109/AUV.2012.6380737.

[12] Scott B. Gibson and Daniel J. Stilwell. An H∞ loop-shaping design procedure for attitude control of an AUV. In *OCEANS 2016 MTS/IEEE Monterey*, pages 1–7, 2016. doi: 10.1109/OCEANS.2016.7761167. doi:10.1109/OCEANS.2016.7761167.

[13] Agathe Girard, Carl Edward Rasmussen, Joaquin Quiñonero Candela, and Roderick Murray-Smith. Gaussian process priors with uncertain inputs application to multiple-step ahead time series forecasting. In *Proceedings of the 15th International Conference on Neural Information Processing Systems*, NIPS'02, page 545–552, Cambridge, MA, USA, 2002. MIT Press. doi: 10.5555/2968618.2968686. doi:10.5555/2968618.2968686.

[14] Prasad Hemakumara and Salah Sukkarieh. Non-parametric UAV system identification with dependent Gaussian processes. In *2011 IEEE International Conference on*

Robotics and Automation, pages 4435–4441, 2011. doi: 10.1109/ICRA.2011.5979728. doi:10.1109/ICRA.2011.5979728.

[15] M. E. Kepler, S. Pawar, D. J. Stilwell, S. Brizzolara, and W. L. Neu. Assessment of AUV hydrodynamic coefficients from analytic and semi-empirical methods. In *OCEANS 2018 MTS/IEEE Charleston*, pages 1–9, 2018. doi: 10.1109/OCEANS.2018.8604584. doi:10.1109/OCEANS.2018.8604584.

[16] Justin T. Kleiber, Lakshmi M. Miller, Stephen Krauss, Daniel J. Stilwell, and Stefano Brizzolara. Assessing the effect of hydrodynamic parameter uncertainty on AUV performance with Gaussian processes. In *OCEANS 2021: San Diego – Porto*, pages 1–6, 2021. doi: 10.23919/OCEANS44145.2021.9705837.

[17] Lionel Lapierre. Robust diving control of an AUV. *Ocean Engineering*, 36(1):92–104, 2009. ISSN 0029-8018. doi: https://doi.org/10.1016/j.oceaneng.2008.10.006. URL `https://www.sciencedirect.com/science/article/pii/S002980180800228X`. doi:10.1016/j.oceaneng.2008.10.006.

[18] Shuang Liu and Dong Sun. Modeling and experimental study for minimization of energy consumption of a mobile robot. In *2012 IEEE/ASME International Conference on Advanced Intelligent Mechatronics (AIM)*, pages 708–713, 2012. doi: 10.1109/AIM.2012.6265887.

[19] D. McFarlane and K. Glover. A loop-shaping design procedure using H_∞ synthesis. *IEEE Transactions on Automatic Control*, 37(6):759–769, 1992. doi: 10.1109/9.256330.

[20] Fabio Morbidi, Roel Cano, and David Lara. Minimum-energy path generation for a quadrotor UAV. In *2016 IEEE International Conference on Robotics and Automation (ICRA)*, pages 1492–1498, 2016. doi: 10.1109/ICRA.2016.7487285.

[21] Taylor Njaka, Lakshmi M Miller, Stefano Brizzolara, and Daniel J Stilwell. Method for improving existing maneuvering models to accommodate large drift angles. In *Global Oceans 2020: Singapore–US Gulf Coast*, pages 1–4. IEEE, 2020.

[22] Taylor Njaka, Stefano Brizzolara, and Daniel J Stilwell. Guide for CFD-informed AUV maneuvering models. *Society of Naval Architects and Marine Engineers*, 2022.

[23] Doug Perrault, Neil Bose, Siu O'Young, and Christopher D. Williams. Sensitivity of AUV response to variations in hydrodynamic parameters. *Ocean Engineering*, 30(6): 779–811, 2003. ISSN 0029-8018. doi: https://doi.org/10.1016/S0029-8018(02)00043-4. doi:10.1016/S0029-8018(02)00043-4.

[24] Jan Petrich. *Improved guidance, navigation, and control for autonomous underwater vehicles: Theory and experiment*. PhD thesis, Virginia Tech, 2009.

[25] Jan Petrich and Daniel J. Stilwell. Robust control for an autonomous underwater vehicle that suppresses pitch and yaw coupling. *Ocean Engineering*, 38(1):197–204, 2011. doi: 10.1016/j.oceaneng.2010.10.007. doi:10.1016/j.oceaneng.2010.10.007.

[26] Carl Edward Rasmussen and Hannes Nickisch. Gaussian processes for machine learning (GPML) toolbox. *The Journal of Machine Learning Research*, 11:3011–3015, 2010.

[27] Carl Edward Rasmussen and Christopher K I Williams. *Gaussian process for machine learning*, chapter Function-space View, page 13–19. The MIT Press, 2006.

[28] Daniel Roper, Catherine A. Harris, Georgios Salavasidis, Miles Pebody, Robert Templeton, Thomas Prampart, Matthew Kingsland, Richard Morrison, Maaten Furlong, Alexander B. Phillips, and Stephen McPhail. Autosub Long Range 6000: A multiple-month endurance AUV for deep-ocean monitoring and survey. *IEEE Journal of Oceanic Engineering*, 46(4):1179–1191, 2021. doi: 10.1109/JOE.2021.3058416.

[29] Kevin M. Ryan, Jesper Kristensen, You Ling, Sayan Ghosh, Isaac Asher, and Liping Wang. A Gaussian Process Modeling Approach for Fast Robust Design With Uncertain Inputs. In *Turbo Expo: Power for Land, Sea, and Air*, volume Volume 7A: Structures and Dynamics, June 2018. doi: 10.1115/GT2018-77007. doi:10.1115/GT2018-77007.

[30] R. Rajita Shenoi, P. Krishnankutty, and R. Panneer Selvam. Sensitivity study of hydrodynamic derivative variations on the maneuverability prediction of a container ship. In *International Conference on Offshore Mechanics and Arctic Engineering*. ASME, May 2015. doi: 10.1115/omae2015-41490. doi:10.1115/omae2015-41490.

[31] J.F. Swindells, J.R. Coe, and T.B. Godfrey. Absolute viscosity of water at 20-degrees-C. *Journal of Research of the National Bureau of Standards*, 48(1):1, 1952. doi: 10.6028/jres.048.001.

[32] H. Söding. Limits of potential theory in rudder flow predictions. *Ship Technology Research*, 45(3):141–155, 1998.

[33] C. K. I. Williams and C. E. Rasmussen. Gaussian processes for regression. In D. S. Touretzky, M. C. Mozer, and M. E. Hasselmo, editors, *Advances in Neural Information Processing Systems 8*. MIT, June 1996. URL `http://publications.aston.ac.uk/id/eprint/651/`. Copyright of the Massachusetts Institute of Technology Press (MIT Press).

[34] Niankai Yang, Dongsik Chang, Matthew Johnson-Roberson, and Jing Sun. Energy-optimal control for autonomous underwater vehicles using economic model predictive control. *IEEE Transactions on Control Systems Technology*, pages 1–14, 2022. doi: 10.1109/TCST.2022.3143366.

Appendices

Appendix A

Full Uncertainty Mappings

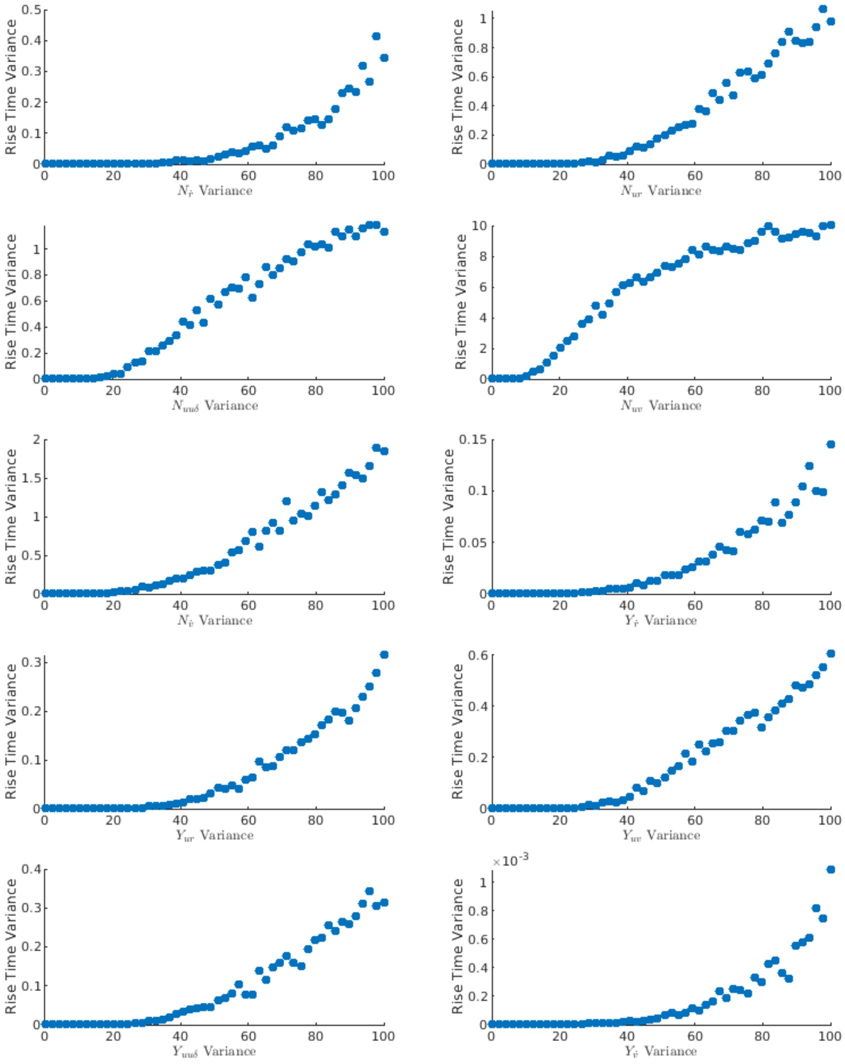

Figure A.1: Rise time variance vs coefficient variance for each coefficient

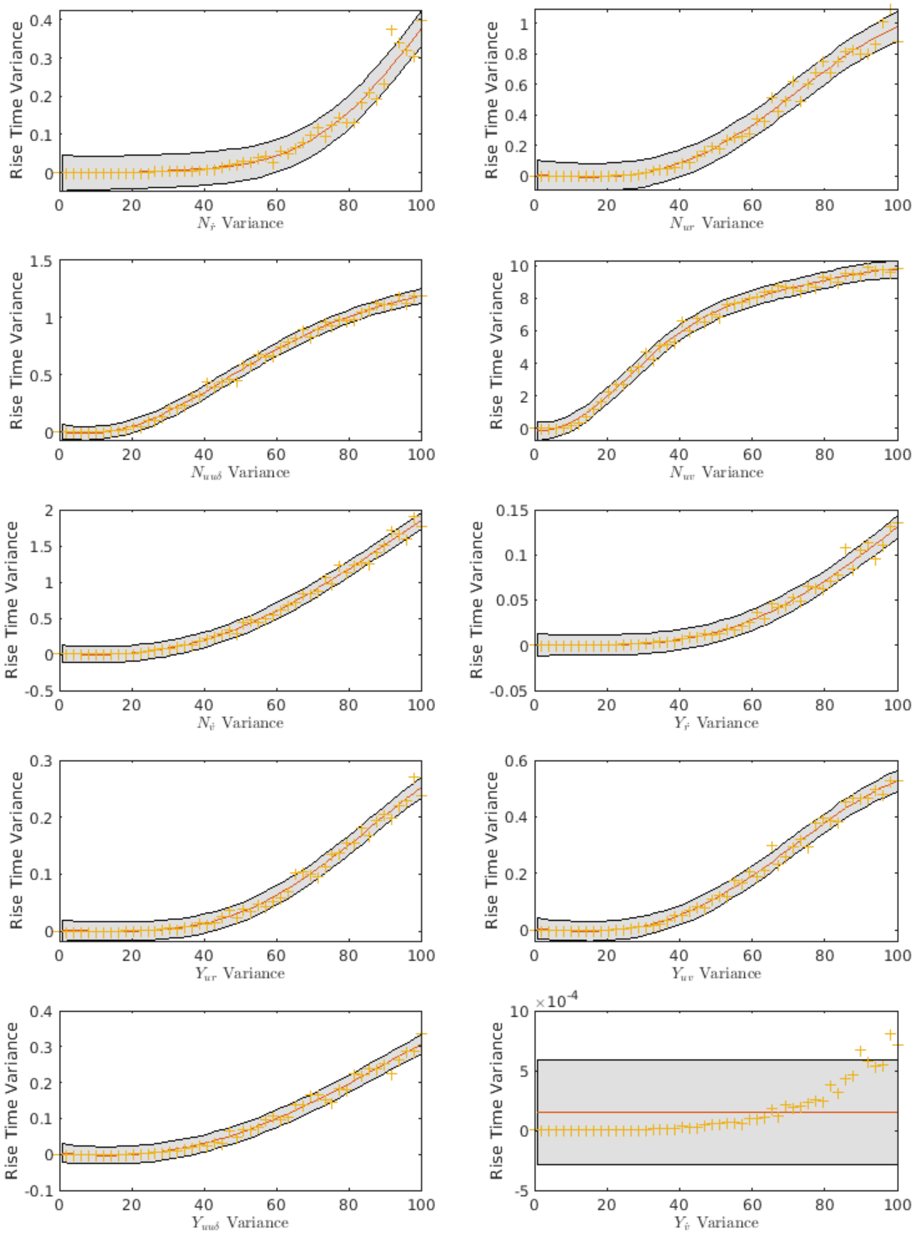

Figure A.2: A GP estimates the rise time variance vs coefficient variance for each coefficient

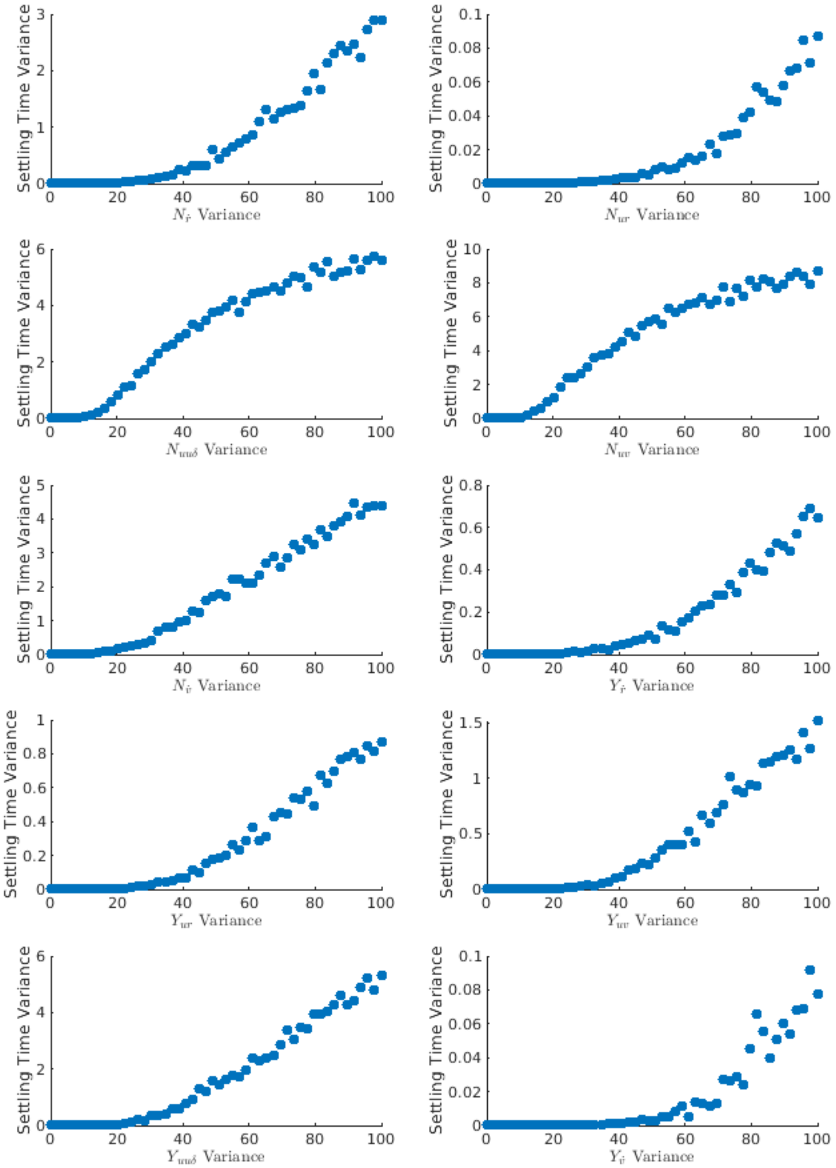

Figure A.3: Settling time variance vs coefficient variance for each coefficient

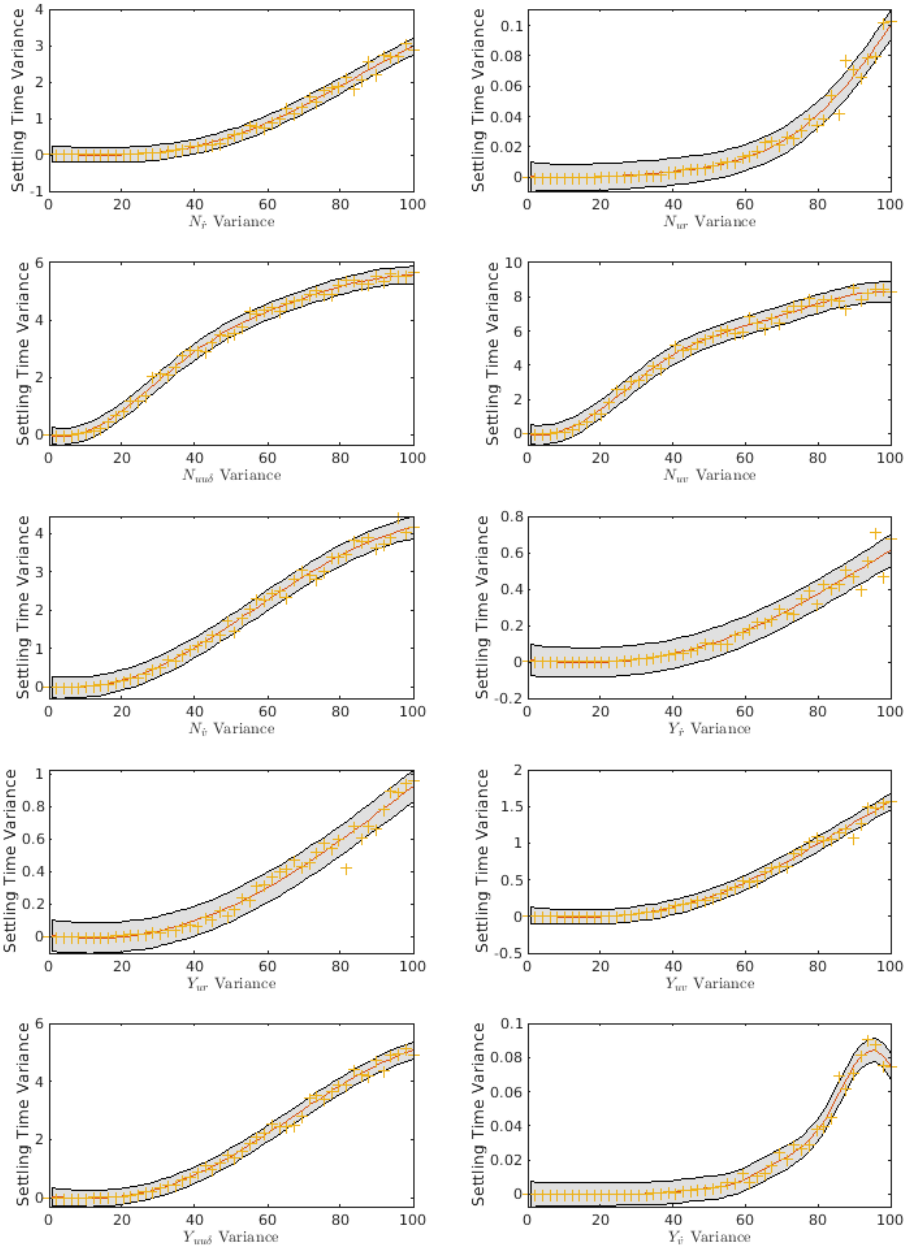

Figure A.4: A GP estimates the settling time variance vs coefficient variance for each coefficient

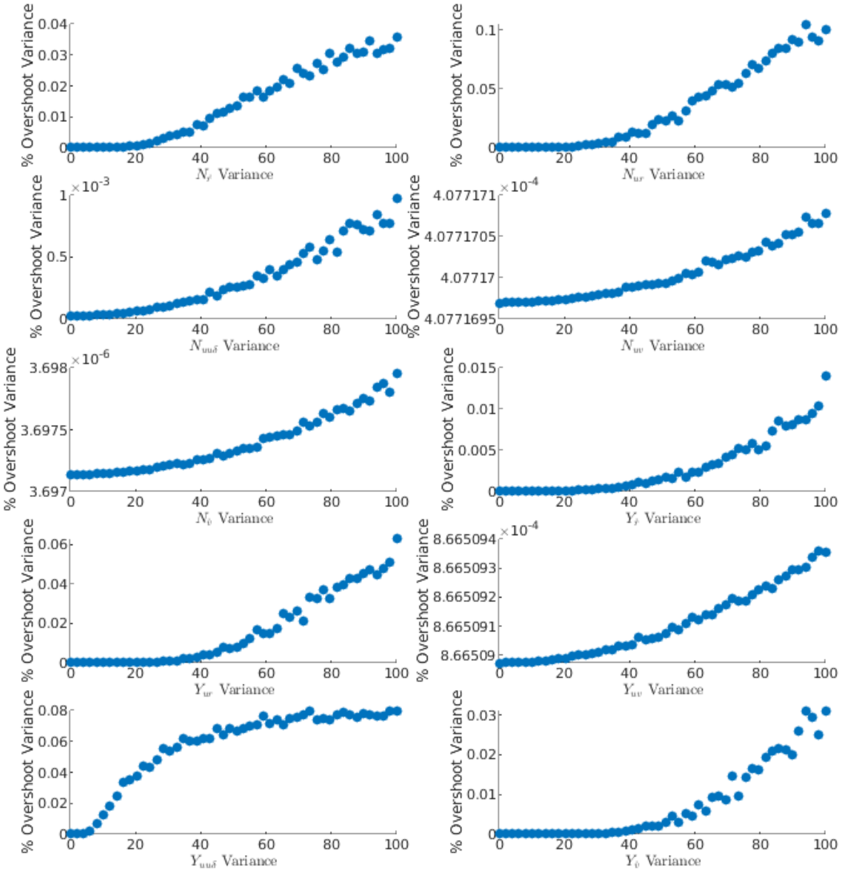

Figure A.5: % overshoot variance vs coefficient variance for each coefficient

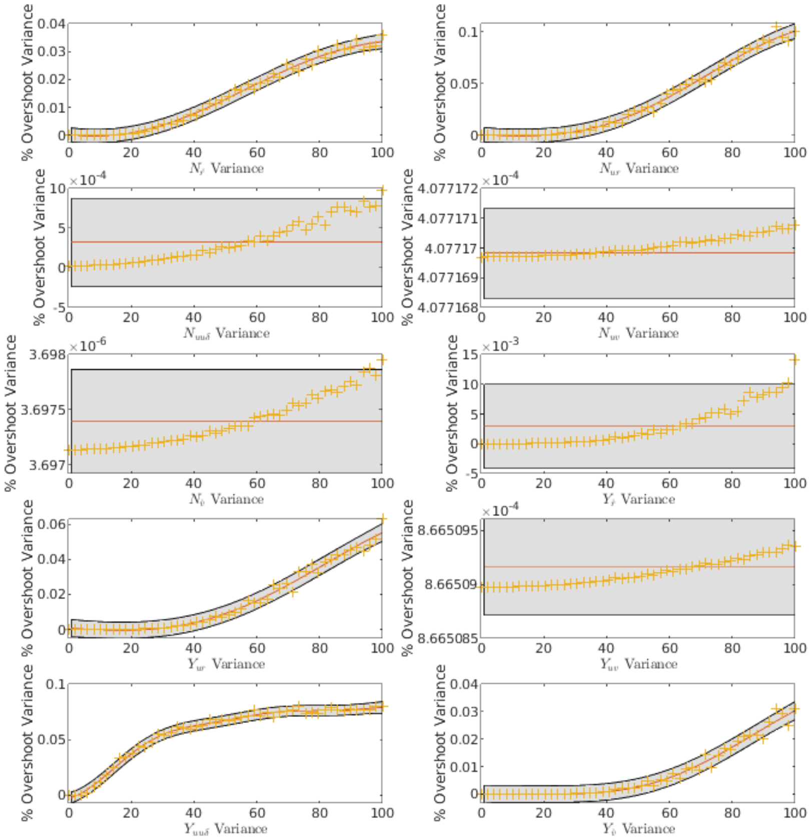

Figure A.6: A GP estimates the % overshoot variance vs coefficient variance for each coefficient

Appendix B

Performance Variance Tables

	Rise Time Variance (sec^2)				
	$N_{\dot{r}}$	N_{ur}	$N_{uu\delta}$	N_{uv}	$N_{\dot{v}}$
N_{ur}	2.96e-06	-	-	-	-
$N_{uu\delta}$	2.48e-06	3.07e-06	-	-	-
N_{uv}	2.82e-06	2.95e-06	3.34e-06	-	-
$N_{\dot{v}}$	2.48e-06	3.94e-06	2.93e-06	2.79e-06	-
$Y_{\dot{r}}$	2.51e-06	3.69e-06	2.17e-06	3e-06	2.82e-06
Y_{ur}	2.42e-06	2.86e-06	2.64e-06	2.89e-06	2.91e-06
Y_{uv}	3.55e-06	3.16e-06	3.36e-06	3e-06	2.66e-06
$Y_{uu\delta}$	2.16e-06	2.69e-06	2.18e-06	3.31e-06	2.58e-06
$Y_{\dot{v}}$	3.36e-06	3.21e-06	3.4e-06	3.09e-06	2.64e-06
	$Y_{\dot{r}}$	Y_{ur}	Y_{uv}	$Y_{uu\delta}$	
Y_{ur}	2.74e-06	-	-	-	
Y_{uv}	2.88e-06	2.48e-06	-	-	
$Y_{uu\delta}$	2.17e-06	2.81e-06	3e-06	-	
$Y_{\dot{v}}$	2.93e-06	2.66e-06	3.66e-06	2.74e-06	

Table B.1: Impact of joint coefficient uncertainties on rise time uncertainty

	Settling Time Variance (sec^2)				
	$N_{\dot{r}}$	N_{ur}	$N_{uu\delta}$	N_{uv}	$N_{\dot{v}}$
N_{ur}	8.51e-05	-	-	-	-
$N_{uu\delta}$	6.97e-05	8.93e-05	-	-	-
N_{uv}	8.06e-05	8.54e-05	9.24e-05	-	-
$N_{\dot{v}}$	6.76e-05	0.000108	8.65e-05	8.13e-05	-
$Y_{\dot{r}}$	7.02e-05	9.56e-05	6.42e-05	8.56e-05	8.38e-05
Y_{ur}	7.18e-05	8.42e-05	7.5e-05	8.19e-05	8.54e-05
Y_{uv}	9.27e-05	9.53e-05	9.03e-05	9.05e-05	9.73e-05
$Y_{uu\delta}$	6.34e-05	8.74e-05	6.2e-05	9.09e-05	7.45e-05
$Y_{\dot{v}}$	0.000104	0.000102	9.86e-05	8.75e-05	7.72e-05
	$Y_{\dot{r}}$	Y_{ur}	Y_{uv}	$Y_{uu\delta}$	
Y_{ur}	7.95e-05	-	-	-	
Y_{uv}	0.000104	7.14e-05	-	-	
$Y_{uu\delta}$	7.13e-05	8.35e-05	8.27e-05	-	
$Y_{\dot{v}}$	8.72e-05	7.66e-05	0.000104	8.29e-05	

Table B.2: Impact of joint coefficient uncertainties on settling time uncertainty

	% Overshoot Variance (%^{2})				
	$N_{\dot{r}}$	N_{ur}	$N_{uu\delta}$	N_{uv}	$N_{\dot{v}}$
N_{ur}	3.23e-05	-	-	-	-
$N_{uu\delta}$	6.44e-06	8.12e-06	-	-	-
N_{uv}	4.6e-06	6.64e-05	2.5e-05	-	-
$N_{\dot{v}}$	7.02e-06	1.16e-05	3.8e-06	0.000308	-
$Y_{\dot{r}}$	5.42e-06	1.12e-05	1.93e-05	0.000345	1.87e-06
Y_{ur}	3.96e-06	6.76e-06	2.52e-06	3.59e-05	1.27e-06
Y_{uv}	0.000198	0.000153	8.81e-05	0.000125	0.000182
$Y_{uu\delta}$	3.57e-06	8.59e-06	4.99e-06	6.4e-05	3.73e-06
$Y_{\dot{v}}$	6.31e-05	1.12e-05	1.11e-05	0.000125	1.31e-05
	$Y_{\dot{r}}$	Y_{ur}	Y_{uv}	$Y_{uu\delta}$	
Y_{ur}	2.69e-06	-	-	-	
Y_{uv}	0.00068	0.000149	-	-	
$Y_{uu\delta}$	8.33e-05	2.79e-06	0.000104	-	
$Y_{\dot{v}}$	1.2e-05	7.08e-05	0.000209	1.6e-05	

Table B.3: Impact of joint coefficient uncertainties on % overshoot uncertainty